國立交通大學

顯示科技研究所

碩士論文

光瞳工程應用於表面電漿激發之研究

Pupil Engineering and Its Applications to Surface Plasma Resonance

研究生：李杰恩

指導教授：田仲豪副教授

中華民國一百零一年七月

光瞳工程應用於表面電漿激發之研究

Pupil Engineering and Its Applications to Surface Plasma Resonance

研究生：李杰恩　　Student：Jie-En Li

指導教授：田仲豪　　Advisor：Chung-Hao Tien

國立交通大學

顯示科技研究所

碩士論文

A Thesis

Submitted to Department of Photonics

College of Electrical and Computer Engineering

National Chiao Tung University

in partial Fulfillment of the Requirements

for the Degree of

Master

in

Department of Photonics

July 2012

Hsinchu, Taiwan, Republic of China

中華民國一百零一年七月

光瞳工程應用於
表面電漿激發之研究

碩士研究生：李杰恩　指導教授：田仲豪

國立交通大學

顯示科技研究所

摘要

根據觀測材料的特性與尺度的大小，繞射理論可以分成將電磁場視為純量之繞射理論或滿足電磁波之邊界條件，計算上較為複雜的向量繞射理論。在傳統低數值孔徑的架構下，採用純量繞射即可達到相當接近的近似解；然而，在現代科技的進步下，高數值孔徑的架構對於某些應用是不可或缺的，純量繞射理論得到的近似解已經無法適用於高數值孔徑的架構下，必須以向量繞射的理論去解釋、估算才能得到精確的解。除了入射光瞳之振幅、相位以外，在向量繞射理論中，我們還必須將入射光瞳的極化的影響納入考量，藉此估算出較為精確的三維點擴散函數。

在這篇論文中，首先將探討入射光瞳對於點擴散函數的影響，並在第二章介紹不同的入射光罩與一些基本應用。接著討論不同的極化光在高數值孔徑的系統下會出現何種聚焦場型。並利用徑向極化光能在一金屬-絕緣層的介面中激發表面電漿的性質，達到超解析的效果。再提出一個新的方法創造出多波長非均勻極化的光束，用以激發多波長表面電漿。最後提出一金屬-絕緣層-金屬的結構，增強此系統對於折射率變化的偵測範圍與敏感度。

Pupil Engineering and Its Applications to Surface Plasma Resonance

Master Student: Jie-En Li **Advisor:** Dr. Chung-Hao Tien

Display Institute

National Chiao Tung University

Abstract

In the diffraction theory, scalar diffraction theory is based on specific conditions such as low numerical aperture. The electromagnetic fields are treated as the scalar components to obtain a good approximation by relatively simple mathematics formula. However, it is necessary to use high numerical aperture in many optical systems while the technology was fast developed. Meanwhile, the approximation of scalar diffraction is so unsuitable that we have to use the vector diffraction theory. The Three Dimensional Point Spread Function (3D PSF) is not only dominated by amplitude and phase but polarization of pupil function in vector diffraction theory.

In this thesis, we first study the relationship between pupil function and point spread function. Different kinds of pupil mask will be introduced in chapter 2. Then we discuss different polarized fields and use radial polarization to excite Surface Plasma Resonance (SPR). A new method is proposed to generate a spatially inhomogeneous polarized beam so that a chromatic SPR can be excited in the objective-based setup. Finally, we add a metal-insulator-metal coupler to enhance the performance of this chromatic SPR sensor.

誌謝

首先感謝 田仲豪老師多年來的指導，從大學專題到研讀碩士學位的期間毫不吝嗇地和我分享學習上與人生經歷上的寶貴經驗，在我窮困潦倒時給了我不少建議，讓我能夠順利完成學業及此論文。

再來感謝實驗室中一路帶領我的藍子翔學長，沒有他在工作上的協助與研究上的建議，相信我沒有辦法在這麼短暫的時間內交出這些研究成果。還有在這段路上同樣給予我許多經驗的小陸、健翔、進哥、壯哥、松柏、展燁、家豪、筱儒、議寬與昇勳學長姊們，沒有你們伸出的援手我無法走出那些艱困的時刻。以及一起一路努力到畢業的同伴洪國恩，和孟潔、錫汶、柏宇、張睿、昇達、履安、庭安、皓謙與郁勛等學弟妹們，希望你們都能順利畢業。

也謝謝系辦的助理們，這兩年來若沒有你們的照顧與提供我工讀的機會，減緩了我許多經濟壓力。感謝我其他的好朋友們，因為你們讓我在學習的路上並不孤單

感謝我的父母多年來的栽培與教養，沒有他們的諄諄教誨與大力支持，不會造就現在的我。最後謝謝我的女朋友，在這麼長的時間裡陪我經歷不少風風雨雨，克服一次又一次的大風大浪，在此，將畢業的喜悅分享給大家。

Table of Contents

Figure Captions

List of Table

Chapter 1

Introduction

Diffraction has been defined as "*any deviation of light rays from rectilinear propagation which cannot be interpreted by either refraction or reflection*" by Sommerfeld[1]. The diffraction theory can be divided into two aspects: scalar or vectorial. Differenceis based on treating electromagnetic wave as a scalar phenomenon or not. In this chapter, the detail of these two diffraction theories will be given.

1.1 Scalar diffraction theory

Classical scalar diffraction theory does not solve the boundary condition problem but a boundary value problem. Most important, light is treated as a scalar phenomenon, neglecting the fundamentally vectorial nature of the electromagnetic fields. Such approaches have certain simplifications and approximations; it means that it is able to describe diffraction of light via a simple mathematical formula, because all components of the electric and magnetic field having identical behavior which is fully described by a single wave equation [1].

It should be started at the Maxwell equation

$$\nabla \cdot \epsilon \vec{E} = 0 \qquad (1.1a),$$

$$\nabla \cdot \mu \vec{H} = 0 \qquad (1.1b),$$

$$\nabla \times \vec{E} = -\mu \frac{\partial \vec{H}}{\partial t} \qquad (1.1c),$$

$$\nabla \times \vec{\mathrm{H}} = \epsilon \frac{\partial \vec{\mathrm{E}}}{\partial \mathrm{t}} \qquad (1.1d).$$

Assuming the propagation medium is linear, isotropic, homogeneous, non-dispersive and nonmagnetic, then we applying the $\nabla \times$ to the Eq. (1.1c) and (1.1d)

$$\nabla \times \left(\nabla \times \vec{H}\right) = \epsilon \frac{\mathrm{d}(\nabla \times \vec{E})}{\mathrm{dt}} \qquad (1.2a),$$

$$\nabla \times \left(\nabla \times \vec{E}\right) = -\mu \frac{\mathrm{d}(\nabla \times \vec{H})}{\mathrm{dt}} \qquad (1.2b).$$

Substitution the Eq. (1.1d) into Eq. (1.2a) and Eq. (1.1c) into Eq. (1.2b) yields

$$\nabla^2 \vec{H} - \frac{n^2}{c^2} \frac{\partial^2 \vec{H}}{\partial t^2} = 0 \qquad (1.3a),$$

$$\nabla^2 \vec{E} - \frac{n^2}{c^2} \frac{\partial^2 \vec{E}}{\partial t^2} = 0 \qquad (1.3b).$$

Where *n* is the refractive index of the propagation medium, defined by

$$\mathrm{n} = \left(\frac{\epsilon}{\epsilon_0}\right)^{1/2} \qquad (1.4).$$

And *c* is the speed of light in vacuum, defined by

$$\mathrm{c} = \frac{1}{\sqrt{\mu_0 \epsilon_0}} \qquad (1.5).$$

Since the Eq. (1.3a) and Eq. (1.3b) can apply for both electric and magnetic field. We can use a single scalar variable $\mathrm{u}(P,t)$ to replace

$$\nabla^2 \mathrm{u}(P,t) - \frac{n^2}{c^2} \frac{\partial^2 \mathrm{u}(P,t)}{\partial t^2} = 0 \qquad (1.6),$$

where $\mathrm{u}(P,t)$ depends on *P* in space and *t* in time.

We have assumed that propagation medium is linear, isotropic, homogeneous, non-dispersive and nonmagnetic so far. Under this condition we can treat the EM field as a scalar field to simplify the calculation. The mathematics is well treated by Fourier analysis.

1.1.1 Kirchhoff diffraction formula

The Kirchhoff diffraction theory shows that the Huygens-Fresnel principle may be regarded as an approximation from of a certain integral theorem which expresses the solution of the homogeneous wave equation, at an arbitrary point in the field, in terms of the values of the solution and its first derivatives at all points on an arbitrary closed surface surrounding *P*[2].

We consider first a strictly monochromatic scalar wave

$$u(x,y,z,t) = U(x,y,z)e^{-i\omega t} \tag{1.7}$$

The space-dependent part in Eq. (1.7) satisfies the time-independent wave equation in vacuum

$$(\nabla^2 + k^2)U = 0 \tag{1.8},$$

where $k = {}^{\omega}/_{c}$. This equation is well known as the Helmholtz equation.

Let *V* be a volume bounded by a closed surface *S*, and *P* be any point within it; we have by Green's theorem

$$\iiint_V (U\nabla^2 G - G\nabla^2 U)dV = \iint_{S_1+S_2}(U\frac{\partial G}{\partial n} - G\frac{\partial U}{\partial n})dS \tag{1.9},$$

where *n* is the outward normal direction at each point on *S*. *U* and *G* are any function of positions shown in Fig. 1-1.

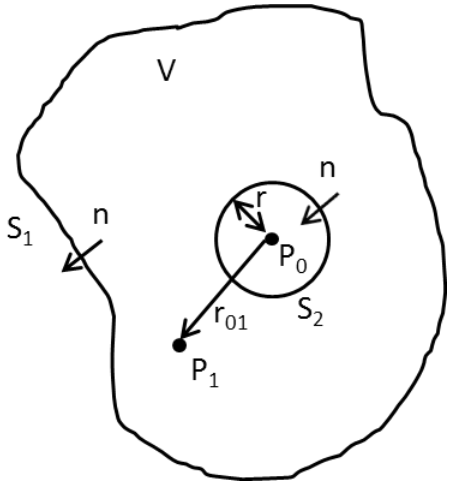

Fig. 1-1 Surface of integration.

Assuming *U* and *G* satisfy the Helmholtz equation

$$(\nabla^2 + k^2)U = 0 \qquad (1.10a),$$

$$(\nabla^2 + k^2)G = 0 \qquad (1.10b).$$

Substituting the Eq. (1.10a) and Eq. (1.10b) in the Eq. (1.9), we obtain

$$\iint_{S_1+S_2} \left(U\frac{\partial G}{\partial n} - G\frac{\partial U}{\partial n}\right) dS = 0 \qquad (1.11).$$

Assuming we have a point source at P_0, then for a general point P_1 on *S*, we have

$$\mathrm{G(P_1)} = \frac{\exp(jkr_{01})}{r_{01}} \qquad (1.12a)$$

and

$$\frac{\partial \mathrm{G(P_1)}}{\partial \mathrm{n}} = \cos(\vec{n}, \overrightarrow{r_{01}}) \left(jk - \frac{1}{r_{01}}\right) \frac{\exp(jkr_{01})}{r_{01}} \qquad (1.12b)$$

where r_{01} is the length of vector $\overrightarrow{r_{01}}$ which points from P_0 to P_1. For a particular case of P_1 on S_2, $\cos(\vec{n}, \overrightarrow{r_{01}}) = -1$, Eq. (1.12a) and Eq. (1.12b) become

$$\mathrm{G(P_1)} = \frac{\exp(jkr)}{r} \qquad (1.13a)$$

and

$$\frac{\partial \mathrm{G(P_1)}}{\partial \mathrm{n}} = \left(\frac{1}{r} - jk\right) \frac{\exp(jkr)}{r} \qquad (1.13b).$$

Letting r become arbitrarily small, the continuity of *U* at P_0 allows us to write

$$\lim_{r\to 0} \iint_{S_2} \left(U\frac{\partial \mathrm{G}}{\partial \mathrm{n}} - G\frac{\partial \mathrm{U}}{\partial \mathrm{n}}\right) ds$$

$$= \lim_{r\to 0} 4\pi r^2 \left[U(P_0)\left(\frac{1}{r} - jk\right)\frac{\exp(jkr)}{r} - \frac{\partial U(P_0)}{\partial \mathrm{n}}\frac{\exp(jkr)}{r}\right] = 4\pi U(P_0) \qquad (1.14).$$

Substituting this result into Eq. (1.11) gets

$$U(P_0) = \frac{1}{4\pi}\iint_{S_1} \left\{\frac{\partial \mathrm{U}}{\partial \mathrm{n}}\left[\frac{\exp(jkr_{01})}{r_{01}}\right] - U\frac{\partial}{\partial n}\left[\frac{\exp(jkr_{01})}{r_{01}}\right]\right\} ds \qquad (1.15).$$

This result is known as the Kirchhoff diffraction formula; it plays an important

role in the development of the scalar diffraction theory, for it allows the field at any point P_0 to be expressed in terms of the "boundary values" of the spherical wave on any close surface surrounding that point.

1.1.2 Fresnel-Kirchhoff diffraction formula

In typical case, the distance r_{01} in Kirchhoff diffraction formula from the aperture to the observation point is much larger than wavelength. That means we have $k \gg 1/r_{01}$, and Eq. (1.12b) become

$$\frac{\partial G(P_1)}{\partial n} \approx jk\cos(\vec{n},\overrightarrow{r_{01}})\frac{\exp(jkr_{01})}{r_{01}} \qquad (1.16).$$

Substitute this result into Eq. (1.15), we get

$$U(P_0) = \frac{1}{4\pi}\iint_{S_1}\frac{\exp(jkr_{01})}{r_{01}}\left[\frac{\partial U}{\partial n} - jkU\cos(\vec{n},\overrightarrow{r_{01}})\right]ds \qquad (1.17).$$

Now considering we have a single point-source which illuminates the aperture A from P_2 to P_1, as shown in Fig. 1-2

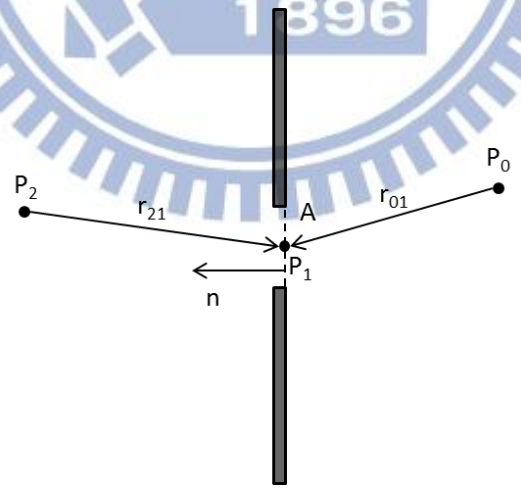

Fig. 1-2 A plane aperture A with point-source illumination

We suppose that the aperture is illuminated by a single spherical wave arising from P_2

$$U(P_1) = \frac{A\exp(jkr_{21})}{r_{21}} \qquad (1.18)$$

and r_{21} is similar to r_{01} which is much larger than wavelength, Eq. (1.17) can be expressed

$$U(P_0) = \frac{A}{i\lambda}\iint_{\mathrm{A}} \frac{\exp[jk(r_{21}+r_{01})]}{r_{21}r_{01}}\left[\frac{\cos(\vec{n},\overrightarrow{r_{01}})-\cos(\vec{n},\overrightarrow{r_{21}})}{2}\right] ds \qquad (1.19).$$

This result only holds for illumination of a single point source, is known as the Fresnel-Kirchhoff diffraction formula.

Above derivation has been restricted to the case which only has an aperture illumination and a single spherical wave. However, such a limitation can be removed by the Rayleigh-Sommerfeld theory.

1.1.3 Rayleigh-Sommerfeld diffraction formula

The Fresnel-Kirchhoff theory has been proved experimentally to yield accurate results and is widely used in practice. However, it shows failure in assuming boundary conditions as the observation point approaches the boundary or aperture. This inconsistency was removed by Sommerfeld so-called Rayleigh-Sommerfeld theory.

If *U* is a boundary value on the screen, *G* must be zero there so that the second term of Green's function in vanishes, similarly, if $\partial U/\partial n$ is the boundary value, $\partial G/\partial n$ must be zero in order to the first term to vanish.

Consider a particular case for a plane screen with an aperture *A* as shown in Fig. 1-3. Green's function is determined by mirror method and formed from the superposition of two spherical waves.

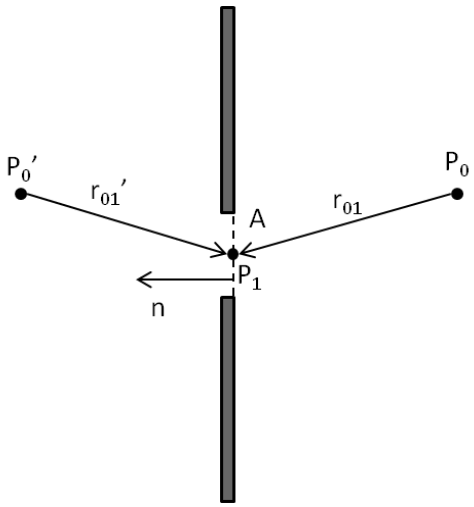

Fig. 1-3 Rayleigh-Sommerfeld diffraction formula for a plane screen

The First Rayleigh-Sommerfeld solution can be found when U is the boundary value. It can be expressed as

$$U_{1st}(P_0) = \frac{-1}{2\pi}\iint_A U\frac{\partial G}{\partial n}\,ds \qquad (1.20).$$

The Second solution can be found if $\partial U/\partial n$ is the boundary value

$$U_{2nd}(P_0) = \frac{1}{2\pi}\iint_A G\frac{\partial U}{\partial n}\,ds \qquad (1.21).$$

Substituting Eq. (1.16) and Eq. (1.18) into Eq. (1.20), we can get

$$U_{1st}(P_0) = \frac{A}{j\lambda}\iint_A \frac{\exp[jk(r_{01}+r_{21})]}{r_{01}r_{21}}\cos(\vec{n},\overrightarrow{r_{01}})\,ds \qquad (1.22)$$

Eq. (1.22) is known as the Rayleigh-Sommerfeld diffraction formula which obeys the Huygens-Fresnel principle. Let us rewrite Eq. (1.22) so that we get a more significant and mathematical form

$$U(P_0) = \frac{1}{j\lambda}\iint_A U(P_1)\frac{\exp(jkr_{01})}{r_{01}}\cos\theta\,ds \qquad (1.23).$$

This result shows that the observed field $U(P_0)$ can be expressed as a superposition of spherical waves emitting from every point P_1 within the aperture *A*.

The scalar diffraction theory had been well developed by Kirchhoff and

Sommerfeld so far. This theory became more complete by Fresnel and Fraunhofer.

1.2 Vector diffraction theory

There are many phenomena that have difference with the approximated result of scalar diffraction theory during the technology was fast developed. For example, scalar diffraction theory cannot explain the focus of electromagnetic fields with polarization[3]. In this section, we will start the vector diffraction theory with the focus computation.

1.2.1 Vectorial Debye theory

We consider an optical system as shown in Fig. 1-4. Two-dimensional pupil coordinates are denoted by (p_x, p_y) and (x, y, z) denote the image coordinates. The field in the exit pupil of this optical system is given and we search the resulting field distribution in the focus.

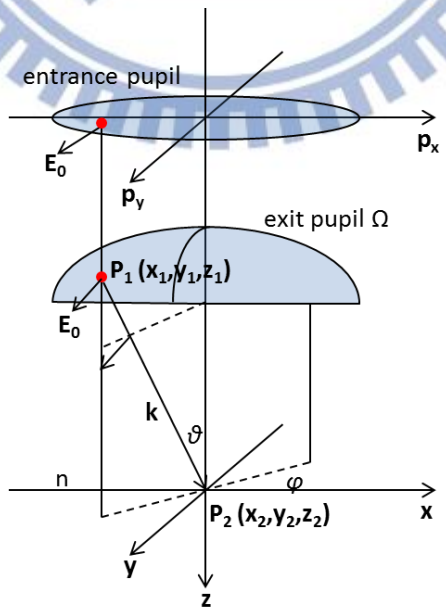

Fig. 1-4 Schematic diagram for focusing system

Assuming $\overrightarrow{E_0}(p_x, p_y)$ is the electric field at the entrance pupil. Considering we have an x-polarization light, the incident electric field at the entrance pupil can be expressed as

$$\vec{E}_i(\rho) = \hat{a}_\rho P(\rho)\cos\varphi - \hat{a}_\varphi P(\rho)\sin\varphi \qquad (1.24)$$

and the electric field at the exit pupil is

$$\begin{aligned}\vec{E}_0(\rho) &= \hat{a}_\rho P(\theta)\cos\varphi - \hat{a}_\varphi P(\theta)\sin\varphi \\ &= P(\theta)\begin{bmatrix}\cos\theta + \sin^2\varphi\cdot(1-\cos\theta)\\ \cos\varphi\sin\varphi\cdot(\cos\varphi - 1)\\ \cos\varphi\sin\theta\end{bmatrix}\end{aligned} \qquad (1.25)$$

where θ and φ are spherical coordinated centered to image space as shown in Fig. 1-5.

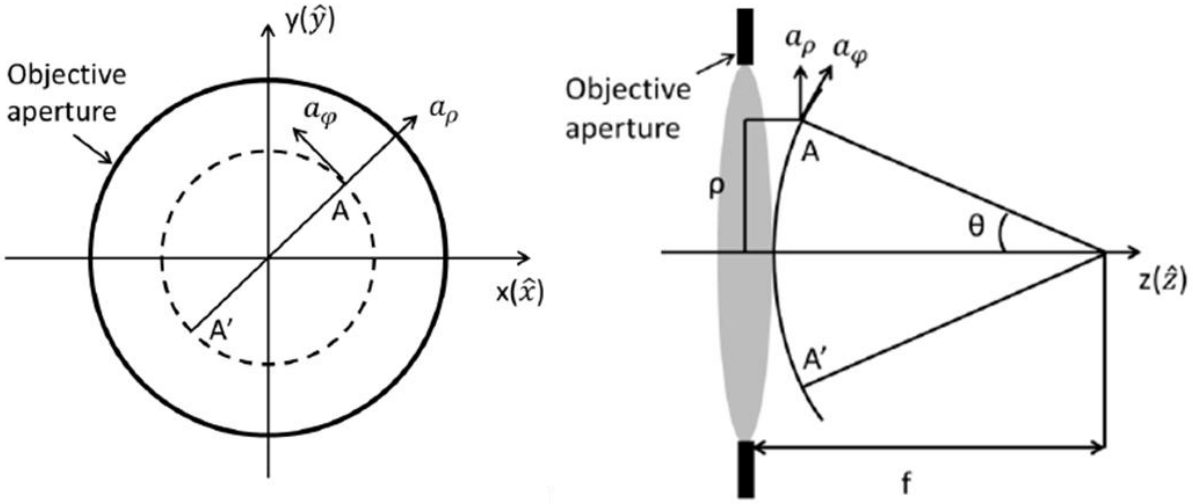

Fig. 1-5 Schematic diagram of $\hat{a}_\rho, \hat{a}_\varphi, \hat{x}$ and $\hat{y}$

For computing the electric field at point P_2in the focal region, we have the Vectorial Debye Integral

$$\vec{\mathrm{E}}(P_2) = \frac{j}{\lambda}\iint_\Omega \overrightarrow{E_0}(P_1)\exp(-j\vec{k}\cdot\vec{R})d\Omega \qquad (1.26)$$

where $\vec{k}$ is the wavevector and $\vec{R}$ is the position vector of P_2 in image

space.$\vec{k}$and$\vec{R}$ can be expressed as

$$\vec{\mathrm{k}} = \begin{bmatrix} \sin\theta\cos\varphi \\ \sin\theta\sin\varphi \\ \cos\theta \end{bmatrix} \quad (1.27a),$$

$$\vec{R} = \begin{bmatrix} x_2 \\ y_2 \\ z_2 \end{bmatrix} = \begin{bmatrix} r_2\cos\Phi \\ r_2\sin\Phi \\ z_2 \end{bmatrix} \quad (1.27b).$$

Substituting Eq. (1.25), Eq.(1.27a) and Eq. (1.27b) into Eq. (1.26), we can get

$$\vec{\mathrm{E}}(r_2, \Phi, z_2) = \frac{j\pi}{\lambda}\begin{bmatrix} I_0 + I_2\cos 2\Phi \\ I_2\sin 2\Phi \\ j\cdot 2I_1\cos\Phi \end{bmatrix} \quad (1.28).$$

Notice that these three variables I_0, I_1 and I_2 are not intensity. The definition of that is given by

$$I_0 = \int_0^\alpha P(\theta)\sin\theta\,(1+\cos\theta)J_0(kr_2\sin\theta)exp(-jkz_2\cos\theta)d\theta \quad (1.29a),$$

$$I_1 = \int_0^\alpha P(\theta)\sin^2\theta\,J_1(kr_2\sin\theta)exp(-jkz_2\cos\theta)d\theta \quad (1.29b),$$

$$I_2 = \int_0^\alpha P(\theta)\sin\theta\,(1-\cos\theta)J_2(kr_2\sin\theta)exp(-jkz_2\cos\theta)d\theta \quad (1.29c)$$

where α is the maximum field of view of the image plane and J_0, J_1 and J_2 are the zero-order, 1st-order and 2nd-order of the1st kind Bessel functions. It is obviously that although the incident field is x-polarized, the field distribution in image space has y- and z-components. This phenomenon will be very important to explain the behavior of focusing field in high-NA system that scalar diffraction theory cannot.

1.2.2 Fresnel's equations

The Fresnel's equations discuss the behavior of light in a planar interface with different polarization. When a plane wave with certain polarization and incident angle θ_i is incident from medium 1 onto the interface between

medium 1 and medium 2 as shown in Fig. 1-6.

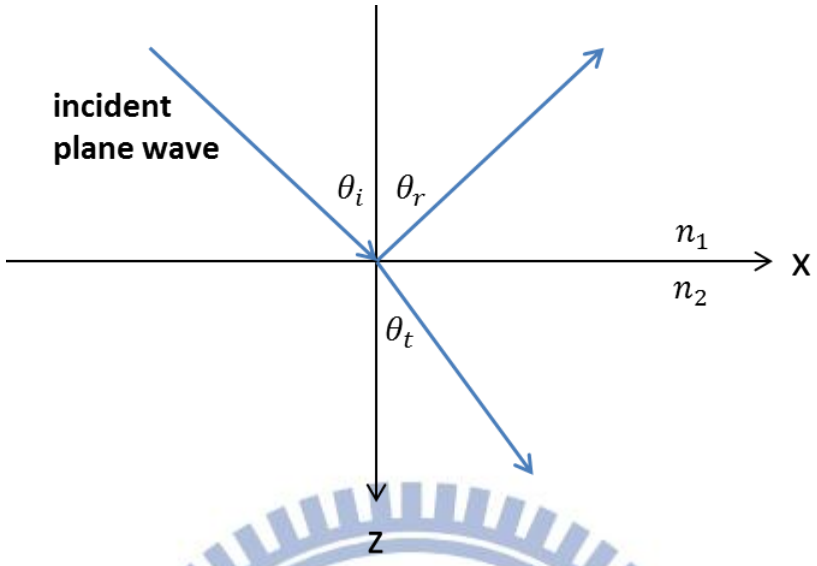

Fig. 1-6 Geometry for Fresnel's equations

The behaviors of different polarization can be regarded as the linear combination of two eigen-modes. One is called s-polarization and another orthogonal polarization is called p-polarization. The field components of these two modes can be expressed as

$$\vec{E} = \begin{bmatrix} 0 \\ E_y \\ 0 \end{bmatrix}, \vec{H} = \frac{-j}{\omega\mu}\nabla \times \vec{E} = \frac{-j}{\omega\mu}\begin{bmatrix} \partial E_y/\partial z \\ 0 \\ -\partial E_y/\partial x \end{bmatrix} \qquad (1.30a)$$

for s-polarization and

$$\vec{H} = \begin{bmatrix} 0 \\ H_y \\ 0 \end{bmatrix}, \vec{E} = \frac{j}{\omega\epsilon}\nabla \times \vec{E} = \frac{j}{\omega\epsilon}\begin{bmatrix} -\partial H_y/\partial z \\ 0 \\ \partial H_y/\partial x \end{bmatrix} \qquad (1.30b)$$

for p-polarization. The tangential fields must be continued at the interface for the boundary conditions. Therefore, we consider an s-polarized plane wave that is propagated with an incident angle θ_i to the z axis. The tangential field components are

$$E_{iy} = \exp[jn_1k_0(x\sin\theta_i + z\cos\theta_i)] \qquad (1.31a),$$

$$H_{ix} = -\frac{n_1 k_0}{\omega\mu}\cos\theta_i \, E_{iy} \qquad (1.31b).$$

According to the law of reflection $\theta_r = \theta_i$, the reflected field becomes

$$E_{ry} = r_s \exp[jn_1 k_0 (x \sin\theta_i - z\cos\theta_i)] \qquad (1.32a),$$

$$H_{rx} = \frac{n_1 k_0}{\omega\mu}\cos\theta_i \, E_{ry} \qquad (1.32b)$$

and the transmitted field

$$E_{ty} = t_s \exp[jn_2 k_0 (x \sin\theta_t + z\cos\theta_t)] \qquad (1.33a),$$

$$H_{tx} = -\frac{n_2 k_0}{\omega\mu}\cos\theta_t \, E_{ty} \qquad (1.33b).$$

The boundary condition at the interface requires

$$E_{iy} + E_{ry} = E_{ty} \; @ \; z = 0 \;\rightarrow 1 + r_s = t_s \qquad (1.34a),$$

$$H_{ix} + H_{rx} = H_{tx} \; @ \; z = 0 \;\rightarrow\; n_1\cos\theta_i - r_s n_1 \cos\theta_i = t_s n_2 \cos\theta_t \qquad (1.34b).$$

For a non-magnetic medium, the solutions of the reflection and transmission coefficients for s-polarization are

$$r_s = \frac{n_1\cos\theta_i - n_2\cos\theta_t}{n_1\cos\theta_i + n_2\cos\theta_t} \qquad (1.35a),$$

$$t_s = \frac{2n_1\cos\theta_i}{n_1\cos\theta_i + n_2\cos\theta_t} \qquad (1.35b).$$

The computation for p-polarization is analogous, resulting the coefficients

$$r_p = \frac{n_2\cos\theta_i - n_1\cos\theta_t}{n_2\cos\theta_i + n_1\cos\theta_t} \qquad (1.36a),$$

$$t_p = \frac{2n_1\cos\theta_i}{n_2\cos\theta_i + n_1\cos\theta_t} \qquad (1.36b).$$

1.3 Motivation of this thesis

Due to the dimension of engineering was reduced down to the order comparable with the wavelength, more complete treatment based on vectorial diffraction shall be considered. Polarization status plays an important role in current optical engineering. Different states of polarization would lead to different effects in the matter-light interaction. Therefore, the scalar diffraction theory is no longer suitable anymore and will be replaced with the vector diffraction theory which can fully explain the characteristic of polarization of light. In this thesis, we will discuss the influence of pupil mask in focus fields. As the consequence, pupil engineering applicable for different purposes was investigated.

The first part of this thesis will discuss the diffraction of lens and the relation between the field distribution at pupil with certain mask and point spread function (PSF). Meanwhile, we will introduce a mathematical tool called Wignerdistribution function (WDF) which represents an optical field in terms of a ray picture [4]. After that, three types of pupil mask will be discussed.

In order to realize the effects of polarization in the focus field, we introduce four kinds of polarization. The focus field with different polarization will be given based on the result in chapter 2.

Then we choose a specific polarization which can be used to excite the Surface Plasmon Resonance (SPR) via objective-based system in the third part of this thesis. Some experimental results will be given.

Finally, we conclude this thesis and provide suggestions for future research toward a continuation of the work presented here.

Chapter 2

Characterization of the Point Spread Function by Pupil Mask

The most important components of optical imaging and data processing systems are lenses. While a thorough discussion of the properties of lenses in geometrical optics would require a rather lengthy detour. The philosophy of our approach in this chapter is to use wave optics analyses of the systems of interest. Furthermore, we will describe the optical fields a by means of a Wigner Distribution Function (WDF) when the optical signals and systems can be described by quadratic-phase functions in particular.

The effects of pupil mask are the topic of Sec. 2.2. Different kinds of pupil mask and its characteristics will be given and elucidated with some optical examples. Sec. 2.2.1 is devoted to the amplitude and phase filter which are generally used in current optical systems. The following section treats the polarizer as a filter, and then discusses the vector point spread function and closes this chapter.

2.1 Diffraction by lens

In this section, we will consider the detail of the light field near the focal region of a lens. Considering we have a field distribution in the focal region, i.e. at $z = f$, as shown in Fig. 2-1. Suppose that a plane wave with amplitude U_0 incident upon the lens. Thus the field distribution in the plane before the lens is $U_1(x_1, y_1) = U_0$. The lens is just like a modulator which modulates the

wave-front by a complex transmittance

$$t(x,y) = P(x,y)\, exp\left[-j\frac{k(x^2+y^2)}{2f}\right] \qquad (2.1)$$

where the quadratic phase factor is the phase transformation of ideal lens. It will be found others phase term if the lens or the pupil has any aberrations.

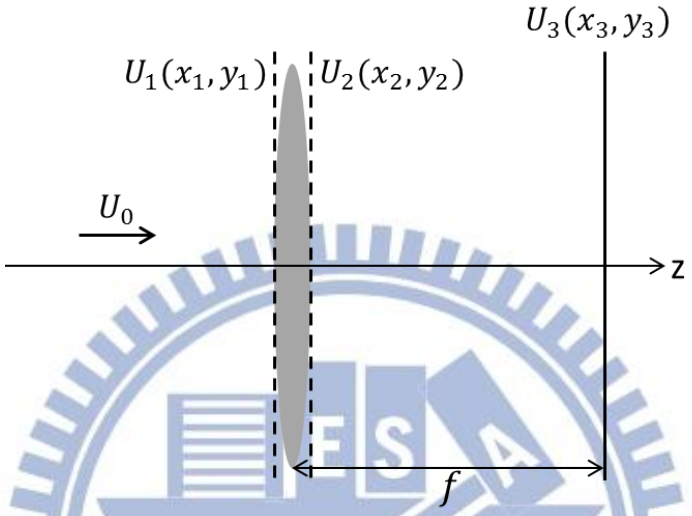

Fig. 2-1 Schematic diagram of diffraction by a lens

Therefore, the field distribution behind the lens is

$$U_2(x_2,y_2) = U_0 \cdot P(x_2,y_2)\, exp\left[-j\frac{k({x_2}^2+{y_2}^2)}{2f}\right] \qquad (2.2).$$

To find the field distribution $U_3(x_3,y_3)$ in the focal region, the Fresnel diffraction formula is applied. Thus,

$$U_3(x_3,y_3) = \frac{e^{j\frac{k}{2f}\left(x_3^2+y_3^2\right)}}{j\lambda f} \times$$

$$\iint_{-\infty}^{\infty} U_2(x_2,y_2)\, e^{j\frac{k}{2f}\left(x_2^2+y_2^2\right)} e^{-j\frac{2\pi}{\lambda f}(x_2x_3+y_2y_3)} dx_2 dy_2 \qquad (2.3)$$

where a constant phase factor e^{jkf} has been dropped. Substituting Eq. (2.2) into Eq. (2.3), the quadratic phase factors of the complex transmittance of lens are seen to exactly cancel, resulting

$$U_3(x_3, y_3) = \frac{U_0 e^{j\frac{k}{2f}\left(x_3^2+y_3^2\right)}}{j\lambda f} \times$$

$$\iint_{-\infty}^{\infty} P(x_2, y_2)\, e^{-j\frac{2\pi}{\lambda f}(x_2 x_3 + y_2 y_3)} dx_2 dy_2 \qquad (2.4)$$

The physical meaning of Eq. (2.4) is obviously seen when we let $f_x = x_3/f\lambda$ and $f_y = y_3/f\lambda$ or, more general, $f_x = x_3/z\lambda$and $f_y = y_3/z\lambda$. Thus the integration part of Eq. (2.4) will be the two-dimensional Fourier transform of the pupil function $P(x, y)$ at spatial frequencies of f_x and f_y as shown below

$$U_3\left(f_x, f_y\right) = \frac{U_0 e^{jkz} e^{j\frac{k}{2z}\left(f_x^2+f_y^2\right)}}{j\lambda f} \times$$

$$\iint_{-\infty}^{\infty} P(x_2, y_2)\, e^{-j\frac{2\pi}{\lambda z}(x_2 f_x + y_2 f_y)} dx_2 dy_2 \qquad (2.5).$$

The quadratic phase term preceded the Fourier transform will be eliminated for very special case $z = f$. Thus the Point Spread Function (PSF) at the focal plane can be simply regarded as a Fourier transform of pupil function $P(x_2, y_2)$. Once again, it should be noticed that the pupil function $P(x_2, y_2)$ is a complex function.

2.1.1 Point spread function

The scalar point spread function has been well discussed by above paragraph. However, in modern technology, the polarization effect is an important role as we mentioned before. Therefore, we will discuss the Vector Point Spread Function (VPSF) in the present section.

The focal field of a polarized pupil was computed in Sec. 1.2.1. In this section we assume that the Jones vector field in the exit pupil stems from the

transmission of an incident homogeneous polarization $\vec{E}_i$ by a Jones matrix pupil $\mathbf{J}(p_x, p_y)$ as shown below

$$\vec{E}(p_x, p_y) = \mathbf{J}(p_x, p_y)\vec{E}_i \tag{2.6}$$

where p_x and p_y are the pupil coordinates.

For a completely polarized illumination, the VPSF is the Fourier transform of the individual vector components after they are transformed by $\boldsymbol{\psi}$ into 3D-space.

$$\vec{E}_{3D} = \boldsymbol{\psi}(p_x, p_y)\mathbf{J}(p_x, p_y)\vec{E}_i \tag{2.7}.$$

Substituting Eq. (2.7) into Eq. (1.26), we can get the VPSF

$$\vec{h}(P_2) = \frac{j}{\lambda}\iint_{\Omega} \boldsymbol{\psi}(p_x, p_y)\mathbf{J}(p_x, p_y)\vec{E}_i \exp(-j\vec{k}\cdot\vec{R})\, d\Omega \tag{2.8}$$

and the intensity of the VPSF is defined as the total intensity of the individual components of the VPSF

$$\mathrm{I}(P_2) = \left\|\vec{h}(P_2)\right\|^2 = \left\|\vec{h}_x(P_2)\right\|^2 + \left\|\vec{h}_y(P_2)\right\|^2 + \left\|\vec{h}_z(P_2)\right\|^2 \tag{2.9}.$$

We will show the field distribution at focus with different input polarization in the next chapter via this equation.

2.1.2 Wigner distribution function

Recently, most optical imaging systems which pursued super resolution used coherent or partially coherent illuminations. In this section, we will introduce the Wigner Distribution Function (WDF) which is directly related to the coherent function and is a powerful and visual description of partially coherent light [5].Considering we have an optical wave as shown in Fig. 2-2

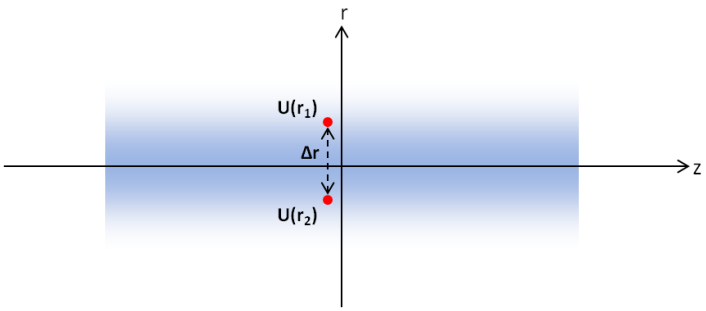

Fig. 2-2 Schematic diagram of WDF

We have the Wigner distribution function

$$W(x,y,u,v) = \iint \Gamma(x,y,x',y') \exp[-j2\pi(x'u + y'v)]\, dx'dy' \quad (2.10)$$

where $\Gamma(x,y,x',y')$ is the mutual coherence function defined by

$$\Gamma(x,y,x',y') = U(x+\frac{x'}{2}, y+\frac{y'}{2}) \cdot U^*(x-\frac{x'}{2}, y-\frac{y'}{2}) \quad (2.11)$$

where $x = (x_1 + x_2)/2\,, y = (y_1 + y_2)/2$ and $x' = x_2 - x_1, y' = y_2 - y_1$ and we have this relation $r_1 = (x_1, y_1)$ and $r_2 = (x_2, y_2)$ as shown in Fig. 2-2.

The mutual coherence function describes the correlation between the optical fields of two different positions. For example, a well coherent light source such as laser has almost same phase at the same wave-front. That means the correlations between two arbitrary points on this wave-front are strong. Other source like LED does not have this characteristic. The phase of different point on the same wave-front is very large and will decrease the mutual coherence function[6].

One of the important characteristics of the WDF is describing position and propagation in the same time. Let us simplify Eq. (2.10) to a 1-dimensional question. Considering there is a point source in the position x_1 and it emerges light field as spherical wave. Then we can use WDF to describe the behavior of light field emerging from that point source as shown in Fig. 2-3.

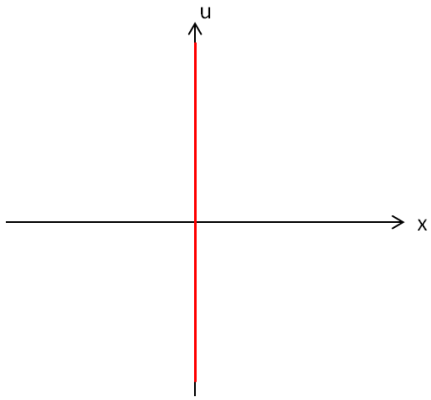

Fig. 2-3 WDF of a point source

If there is a plane wave propagating in the free space. The behavior of this plane wave can be described as shown in Fig. 2-4.

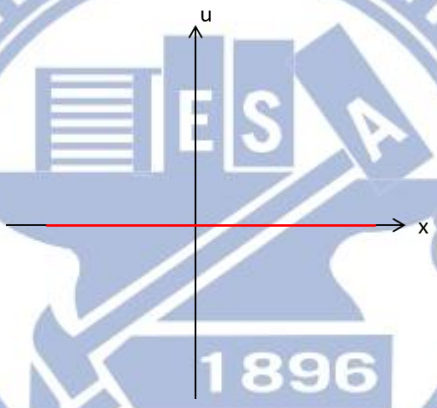

Fig. 2-4 WDF for a plane wave

Finally, we use the WDF to describe an imaging system and end this section. We have a point as object and an imaging system with single lens. Then the WDF of this system can be expressed as shown in the following figure.

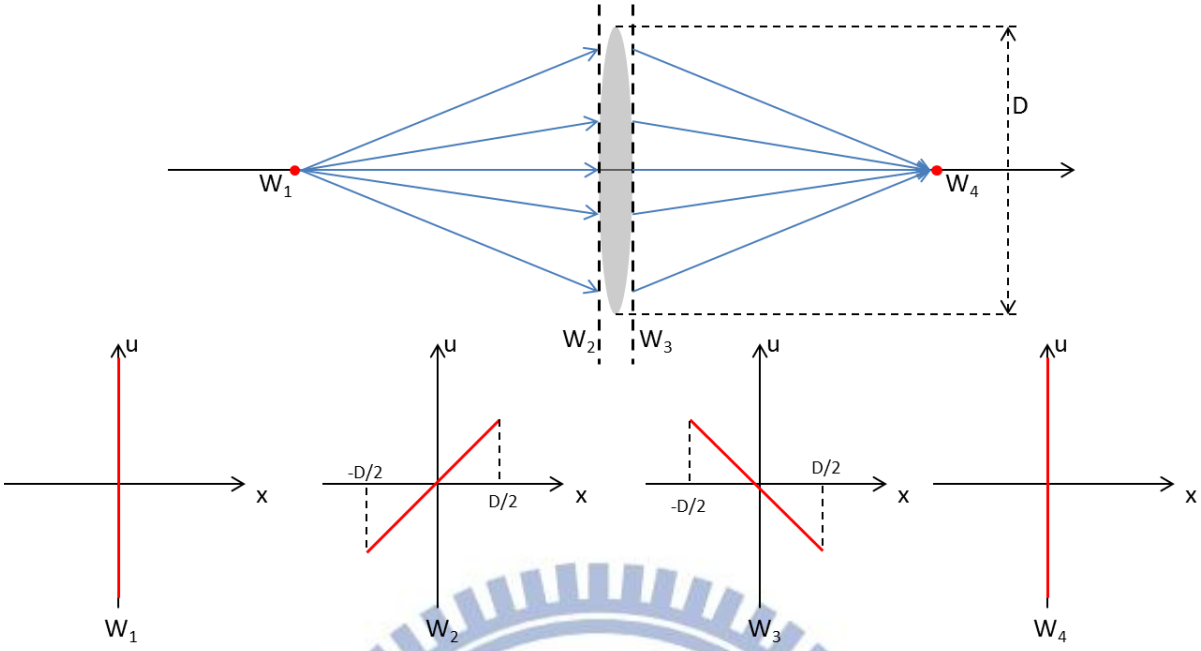

Fig. 2-5 WDF for an imaging system

Here we just consider an ideal imaging system so that there are no aberrations and diffraction. In real case, the WDF will blur because the effects of geometric aberrations or diffraction.

2.2 Pupil Mask

We have discussed the Fourier relationship between pupil function and point spread function in Sec. 2.1.1. Since the output signal of an imaging system is the convolution of the input signal and system's point spread function. By the convolution theorem, the spectrum of output signal is the product of the individual spectra of the input signal and point spread function.

$$F\{g(x)\} = F\{f(x) \otimes h(x)\} = F\{f(x)\} \cdot F\{h(x)\} = F(f_x) \cdot H(f_x) \qquad (2.12)$$

where f is the input signal, h is system's point spread function and g is the output signal and their spectra denoted by capitalization. Eq. (2.12) tells us that the output signal can be modified by the system's point spread function. And we

do know the different pupil function will cause different point spread function. In this section, we will introduce different kinds of pupil mask. The mechanism of modulation of the input field is also called filtering.

2.2.1 Magnitude and phase mask

The transfer function $H(f_x)$ can be expressed as the magnitude part multiplied the phase part

$$H(f_x) = |H(f_x)| \cdot \exp[j\Phi(f_x)] \quad (2.13).$$

The magnitude part $|H(f_x)|$ of the system's transfer function explains the scale factor applied to the amplitude of each sinusoidal component of $f(x)$ and is often called the Modulation Transfer Function (MTF) of the system.Typically, filters which only modulate the magnitude part of transfer function are called "magnitude filter". On the other hand, filters modulate the phase part of transfer function are called "phase filter" or "allpass filter"[7].

Common categories of the magnitude filter include the lowpass filter, highpass filter and bandpass filter. The origin of each name is the working region in the frequency domain. For example, the lowpass filter attenuates or removes the high frequency and conserves the low frequency. A typical lowpass filter is a rectangular function as shown below

$$H(f_x) = RECT(f_x) = \begin{cases} 1, |f_x| \leq \frac{1}{2} \\ 0, \text{otherwise} \end{cases} \quad (2.14).$$

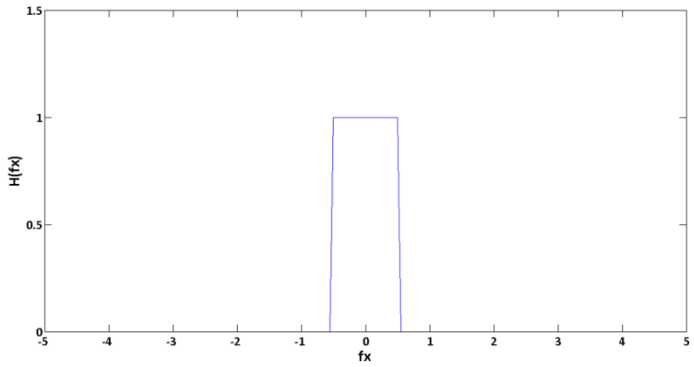

Fig. 2-6 Rectangular function

Considering we have an input signal contained different frequency as shown in Fig. 2-7.

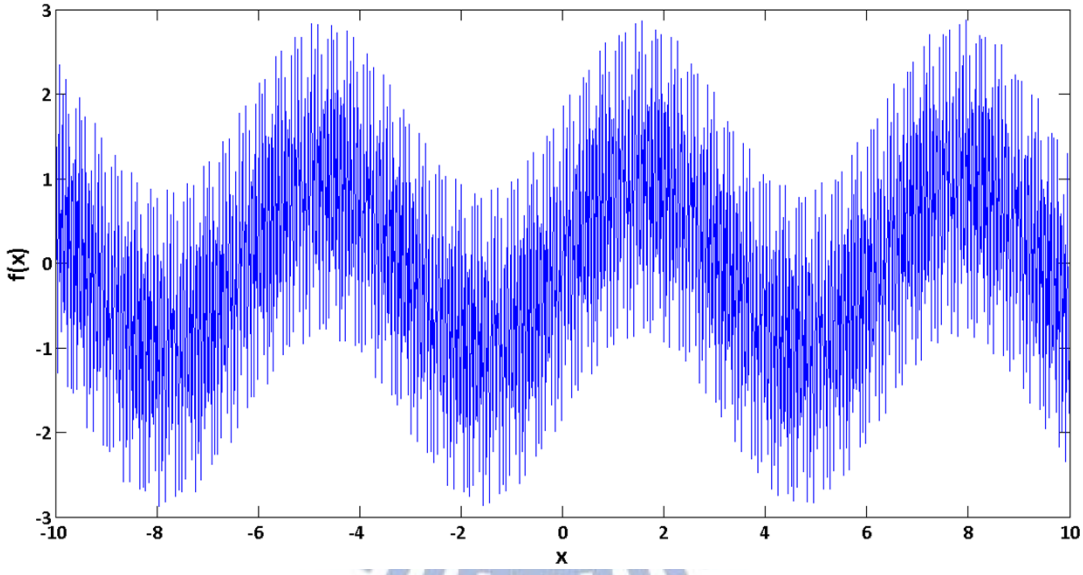

Fig. 2-7 Signal contains different frequency

Then we do the Fourier transform to this signal to get the spectrum of this signal as shown in the following figure

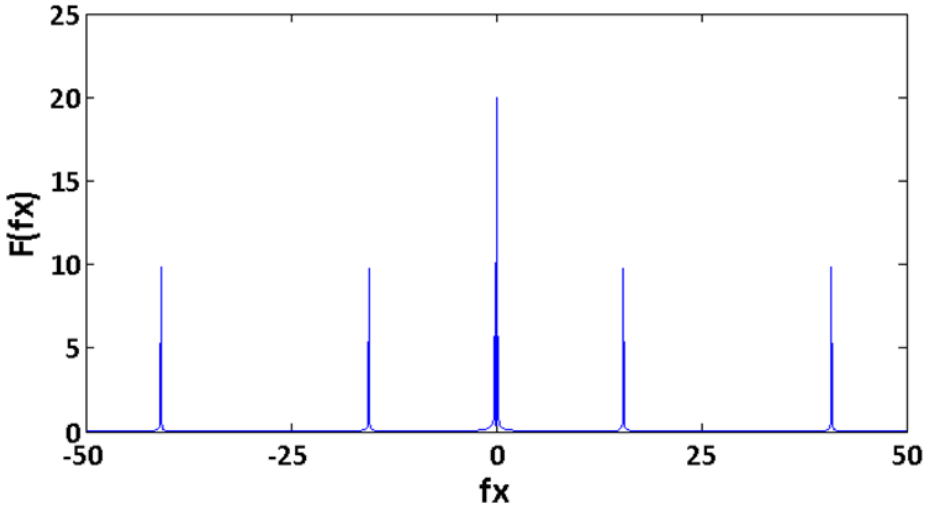

Fig. 2-8 Spectrum of the signal shows in figure 2-7

We can apply different magnitude filter to get different signal depends on our requirement. Here we show a simple result of applying different filter

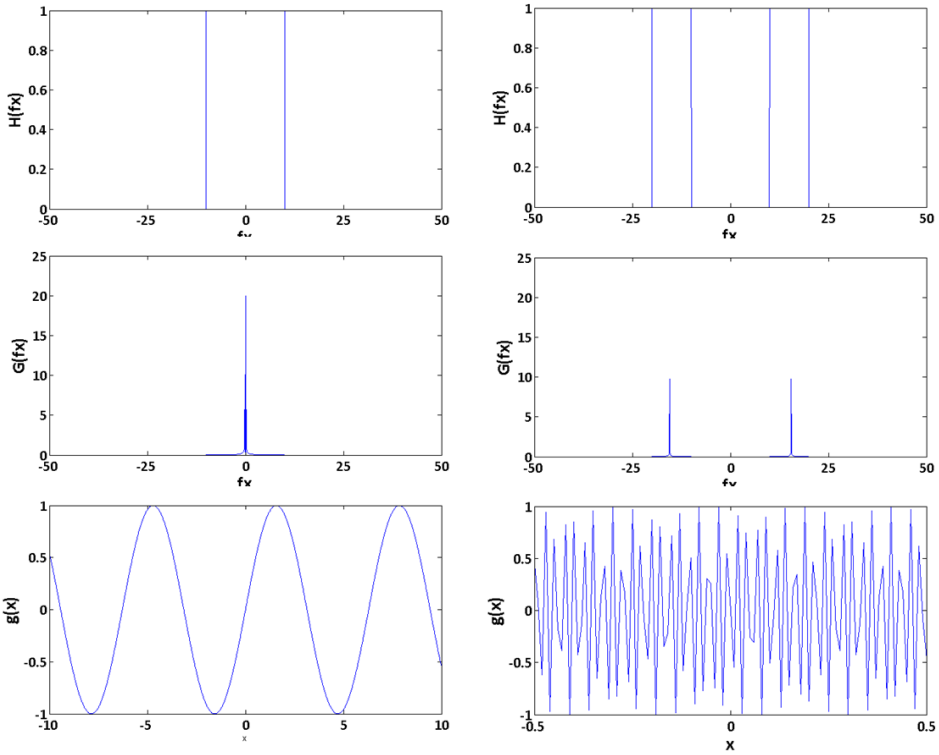

Fig. 2-9 Magnitude filtering

Here is a specific identity worth paying attention. The amplitude of the output signal $g(x)$ is obviously smaller than input signal. This phenomenon conforms to the description we mentioned before because the scale factor of

each sinusoidal component is modified by the transfer function. In other words, the filter of left side of Fig. 2-9 constrains the high frequency components and retains the low frequency; the filter of the other side depresses both high and low frequency terms but middle frequency terms.

Above paragraph discussed the magnitude filter whichremoves components with frequencies outside of the specified band. However, this kind of filter modifies the optical power in the same time. That means we will have poor power at the image plane. Another solution is called phase filter which modifies only the phase of the received wave-front and remains magnitude unchanged.In general, phase filter is designed for particular purpose. The most popular design is E. R. Dowski's Cubic Phase Mask (CPM)[8]. By Goodman's deducing [1], defocus induces a quadratic phase term in the PSF. Applying the CPM at the pupil plane will cause that the PSF remains nearly unchanged in the focus and out of the focus as shown in Fig. 2-10.

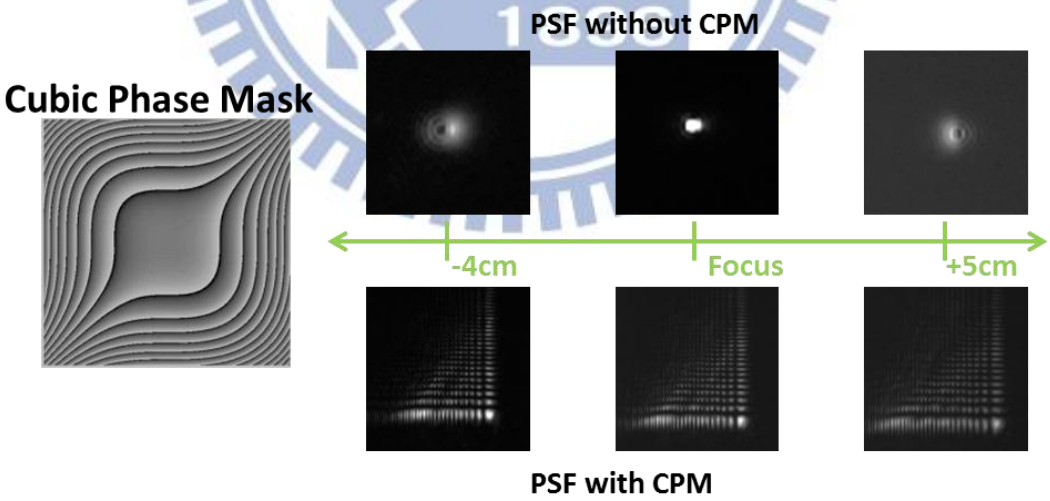

Fig. 2-10 PSF with and without CPM

2.2.2 Polarization mask

Above-mentioned is the common pupil mask and usually used in the low numerical aperture system. Each has specific characterizations and applications. However, as we mentioned before, current technology focuses on the region smaller than the former. Super-resolution microscopy, lithography and other applications are interesting in a tiny area. Therefore, traditional optical mask had faced a huge challenge and was hard to overcome it. Recently, inhomogeneous polarizations are well developed by different generated methods in particular cases [9-13]. One of that is the radially polarized beam. The schematic diagram of the direction of electric fields is shown in the following figure.

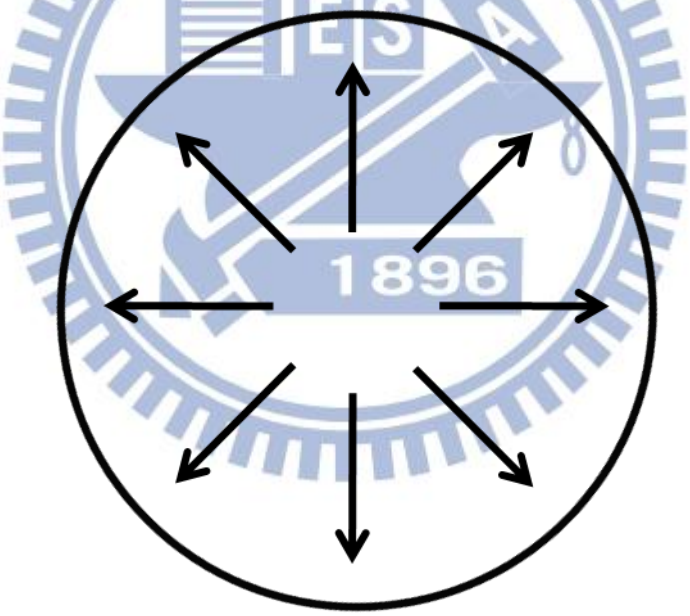

Fig. 2-11 Schematic diagram of radial polarization

In order to further investigate the focusing mechanism of radial polarization, the Vectorial Debye theory was introduced in the Sec. 1.2.1, and the ratio of the longitudinal to transversal component is defined as follows[14]

$$\mathrm{L-T\ ratio} \equiv \frac{Peak\ Intensity\ of\ Longitudinal\ Component}{Peak\ Intensity\ of\ Transversl\ Component} \qquad (2.15)$$

where the coordinates here and we used in Sec.1.2.1 are same.

Focused radially polarized beams with different L-T ratio are shown in the Fig. 2-12.

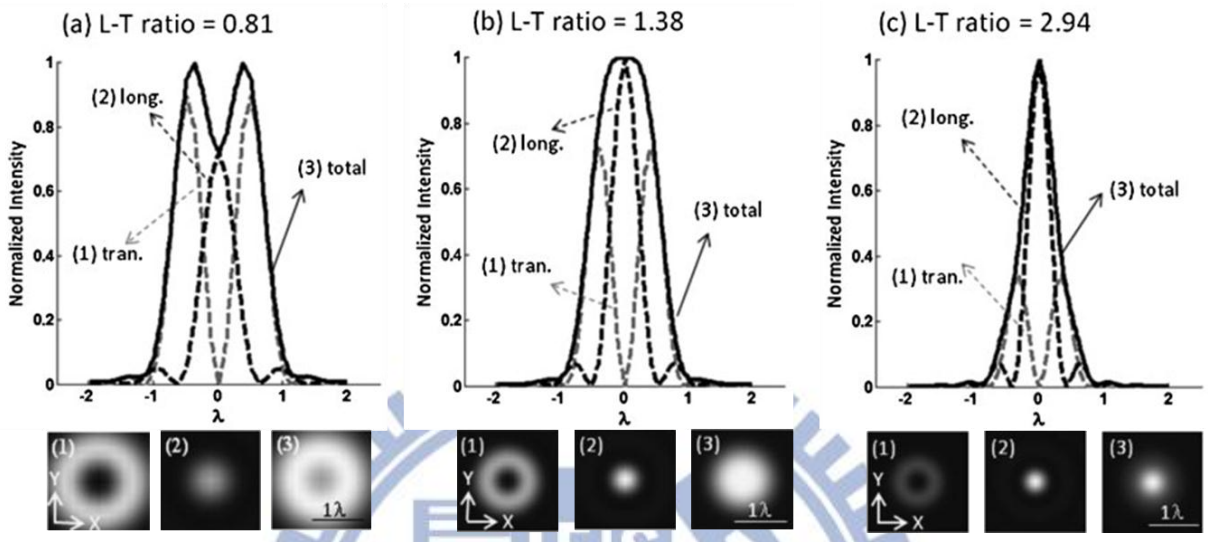

Fig. 2-12 Foci of radially polarized beams with different L-T ratio

One can observe that high L-T ratio radially polarized beam produces a smaller focal spot than other polarization as shown in Fig. 2-13.

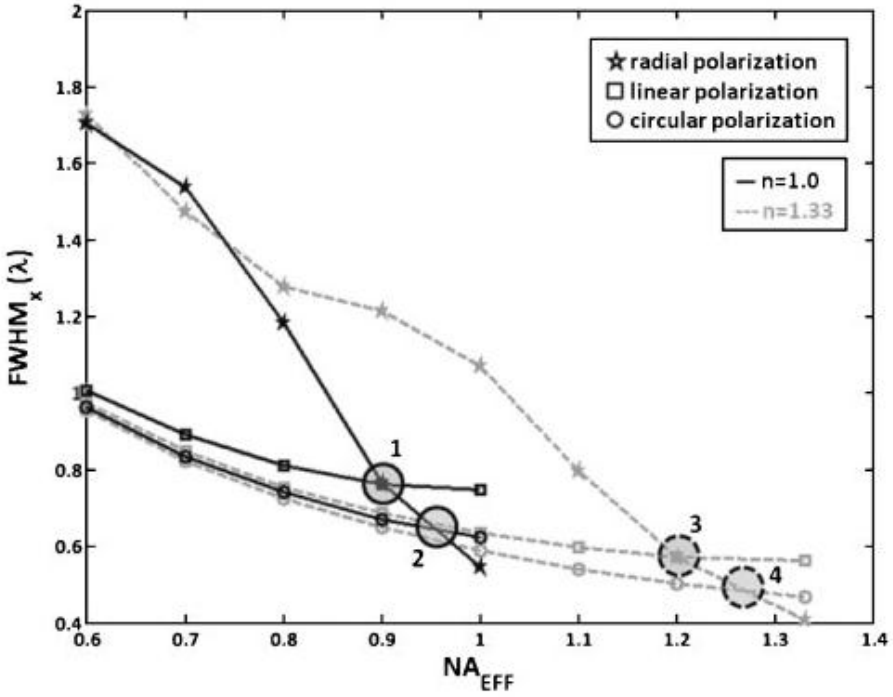

Fig. 2-13FWHM with different polarizations

The Full Width at Half Maximum (FWHM) of high L-T ratio is almost half wavelength. This phenomenon gives us a window to surmount the diffraction-limit. Many applications such as optical tweezers approach a higher resolution via a strongly focal beam with radiallypolarized beam had already proven that the polarization mask can do what traditional mask cannot do. However, once again, the numerical aperture will affect the focus, especially in the high NA system. The more discussion of different polarization in high NA system will be introduced in the following chapter.

2.3 Summary

In this chapter, we discussed different type pupil masks. The input signal can be regarded as a combination of sinusoidal wave with different frequencies and scaling factors. Components with frequencies outside of specific band are removed or depressed in magnitude mask so that causes the optical power smaller. The phase mask adds an additional phase term to each component, and will induce different field distribution but remain the optical power unchanged. The polarization mask provides a window to overcome the natural limit and achieve the super resolution. But it must be noticed that the field distribution will distort because the numerical aperture. We will discuss this effect in the next chapter.

Chapter 3

Polarizations

Polarization means the vibrated direction of the electric field. Different vibrations result in different polarizations. The vibrated direction of electric field can be dominated by the pupil mask. We have discussed the polarization mask in chapter 2. In this chapter, different polarized beams will be introduced. The field distribution in the focus of each polarization will be discussed in high numerical aperture system, too.

3.1 Homogeneous and inhomogeneous polarizations

Generally, homogeneous polarization means that the electric field of every points within the pupil have same direction and inhomogeneous not. The electric field can be described by the two tangential directions (x-y plane) which are perpendicular to the propagated direction (z direction). A y-directional linear polarization means that the electric field of this beam has only y-component. If the electric field has x- and y-component and no phase delay between each component, it is called a 45° linear polarization. The circular polarization represents a beam with 90° phase delay between x- and y-component.

Fig. 3-1 illustrates the difference between homogeneous polarization or not. The arrows represent the vibrated direction of the electric field at each point. For convenience, we use a square aperture to give a simple illustration. But in real case, circular aperture attracts more attention due to its symmetric feature. The calculation of a symmetric aperture is easier than asymmetric.

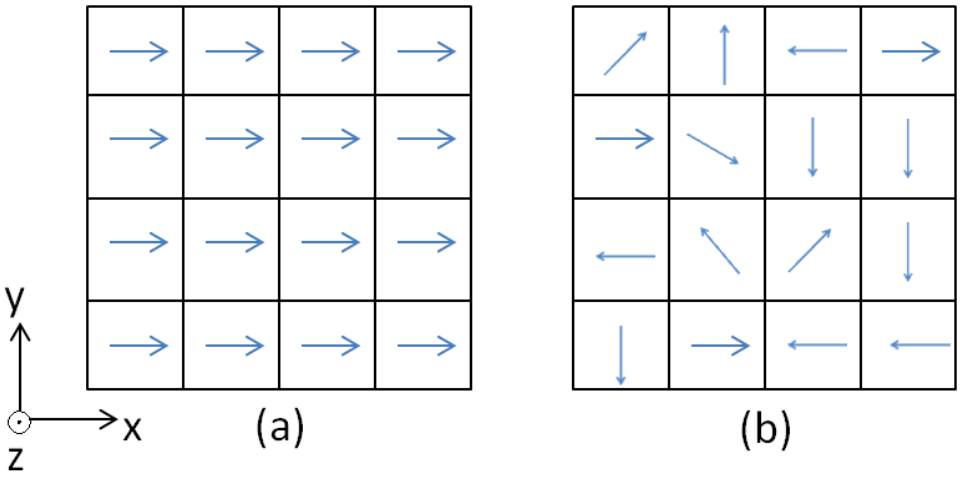

Fig. 3-1 Illustration of (a) homogeneous and (b) inhomogeneous polarization

In a focalizing system, the inhomogeneous polarization can be regarded as a linear combination of two eigenmode: s- and p-polarization as shown in Fig. 3-2.

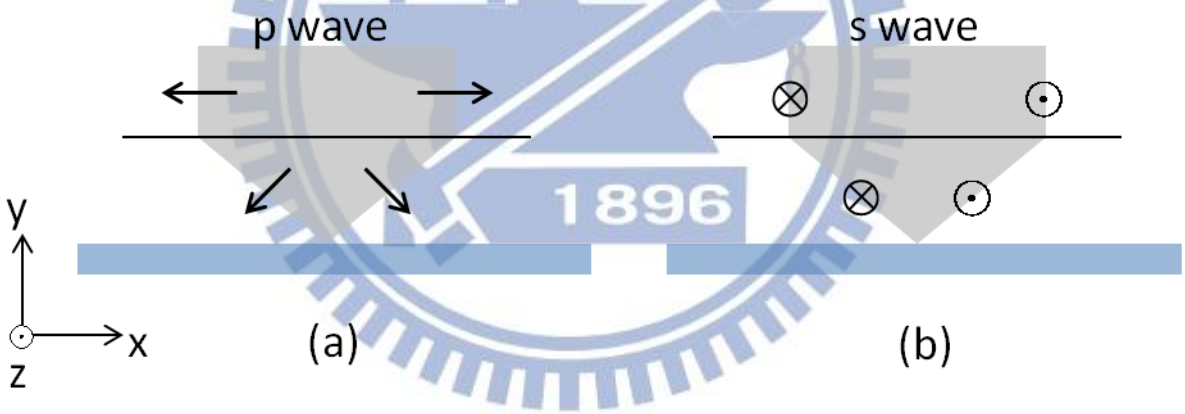

Fig. 3-2 P- and s-polarization for focalizing system

P-wave in focalizing system is an omni-directionally linear polarization along the *r*-direction in cylindrical coordinate, which is called radial polarization. Likewise, the s-wave is called the azimuthal polarization because the vibrated direction of electric field is along the ϕ-direction.

3.2 Polarized beams at the focus

We had introduced different polarizations in the previous section. This section will discuss the focal field of different polarizations with different numerical aperture.

3.2.1 Linear polarization

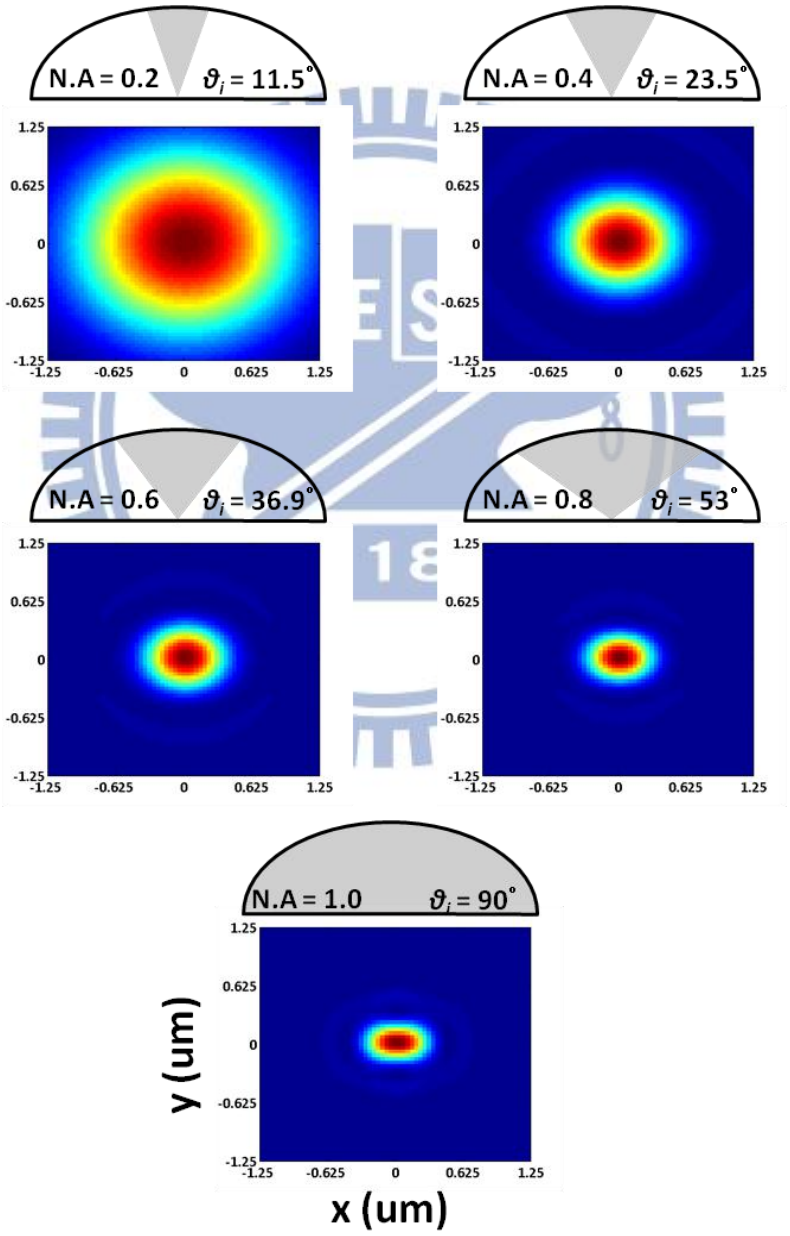

Fig. 3-3 Foci of x-linear polarization with different N.A

Fig. 3-3 illustrates the foci of x-linear polarization with different N.A. It is obviously that the field distribution is “squeezed” along the polarized direction. In order to further discuss this effect, we decompose the total intensity into I_x, I_y and I_z as we mentioned in Sec. 2.1.1. The intensities of each component are demonstrated in the following figure.

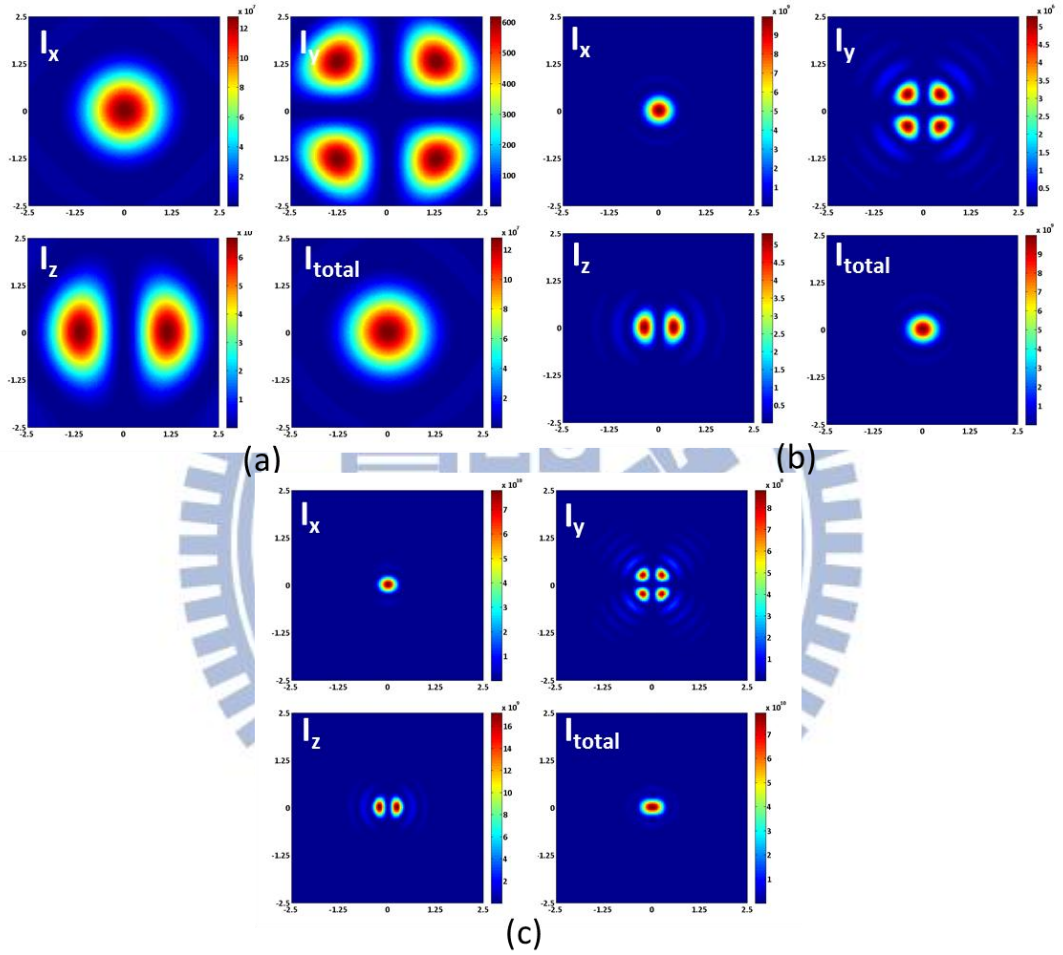

Fig. 3-4 Individual component of foci of x-linear polarization with (a) N.A=0.2 (b) 0.6 (c) 1.0

We can observe that the *y*- and *z*-component are too small to influence the total intensity which is dominated by *x*-component due to the initial polarization is *x*-linear polarization in low N.A. However, *z*-component becomes larger and cannot be neglected when the N.A is increasing. This phenomenon results in a squeezing field distribution in high N.A system.

3.2.2 Circular polarization

The phase delay between *x*- and *y*-component of the incident electric field is $\pm 90°$ called circular polarization. Due to the incident beam has *x*- and *y*-component, we can predict that the "squeezing" effect in linear polarization will be neutralized and the field distribution at the focus will be symmetric. The simulated results indeed demonstrate this prediction as shown in Fig. 3-5.

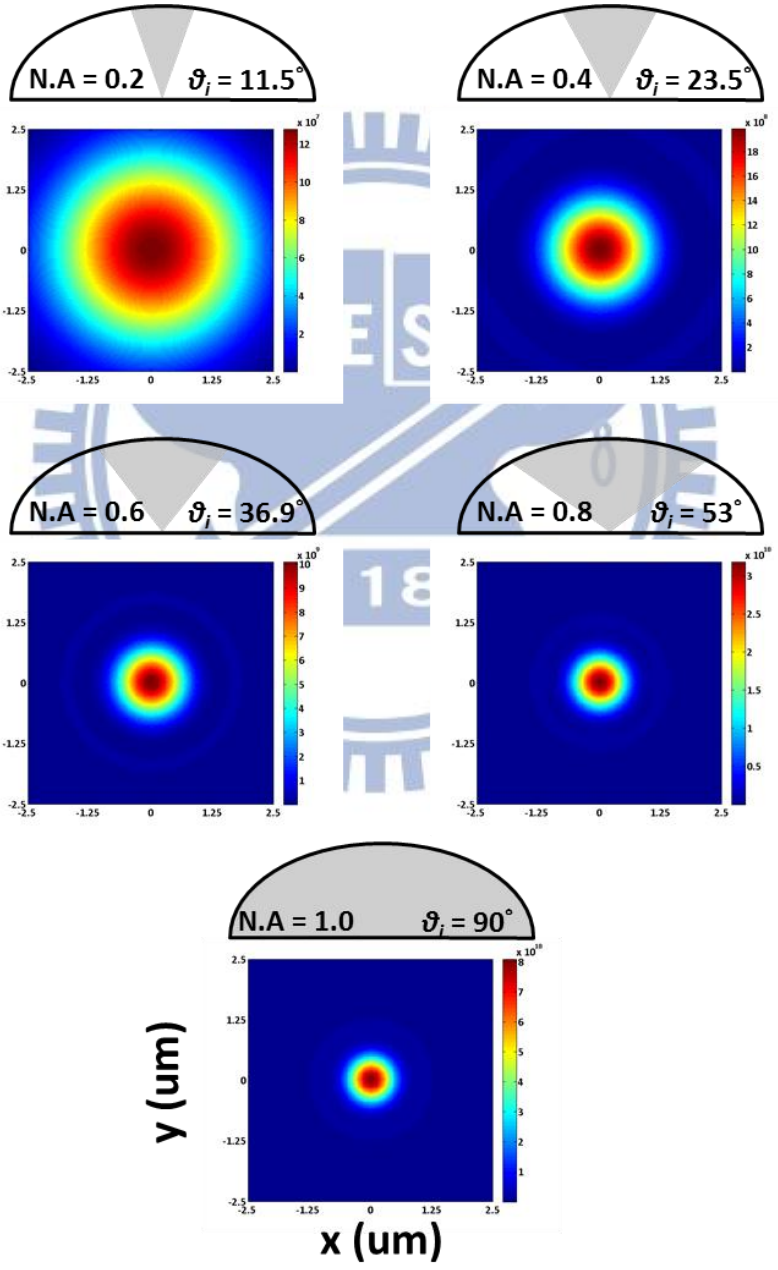

Fig. 3-5 Foci of circular polarization with different N.A

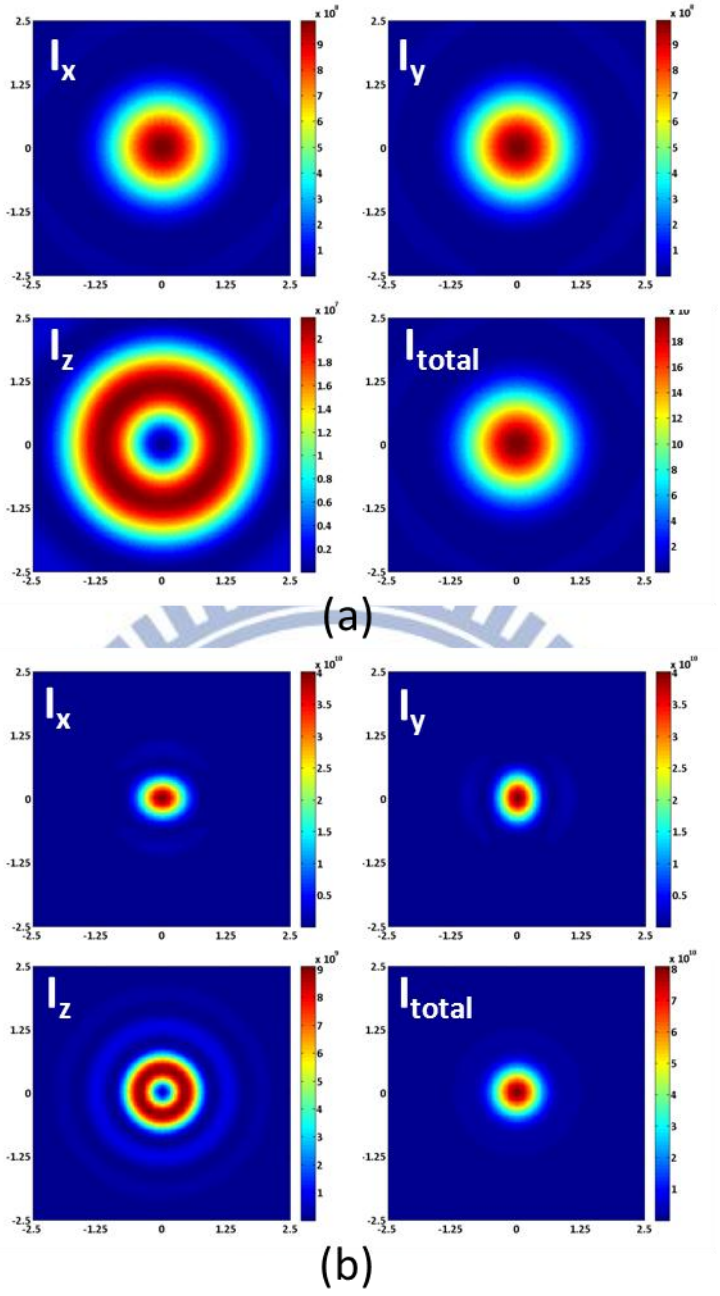

Fig. 3-6 Individual component of foci of circular polarization with (a) N.A = 0.2 (b) 1.0

The intensities of each component are circular symmetric as shown in the above figure. One can observe that the intensities of *x*- and *y*-component are still squeezed but can be neutralized in the total intensity.

3.2.3 Radial polarization

The vibrated direction of electric field along radial direction in cylindrical coordinate is called radial polarization which is an eigenmode of inhomogeneous polarization. As we mentioned before, this kind of polarization will induce a strongly longitudinal component by the in phase interference and lead to a small focus in high N.A system.

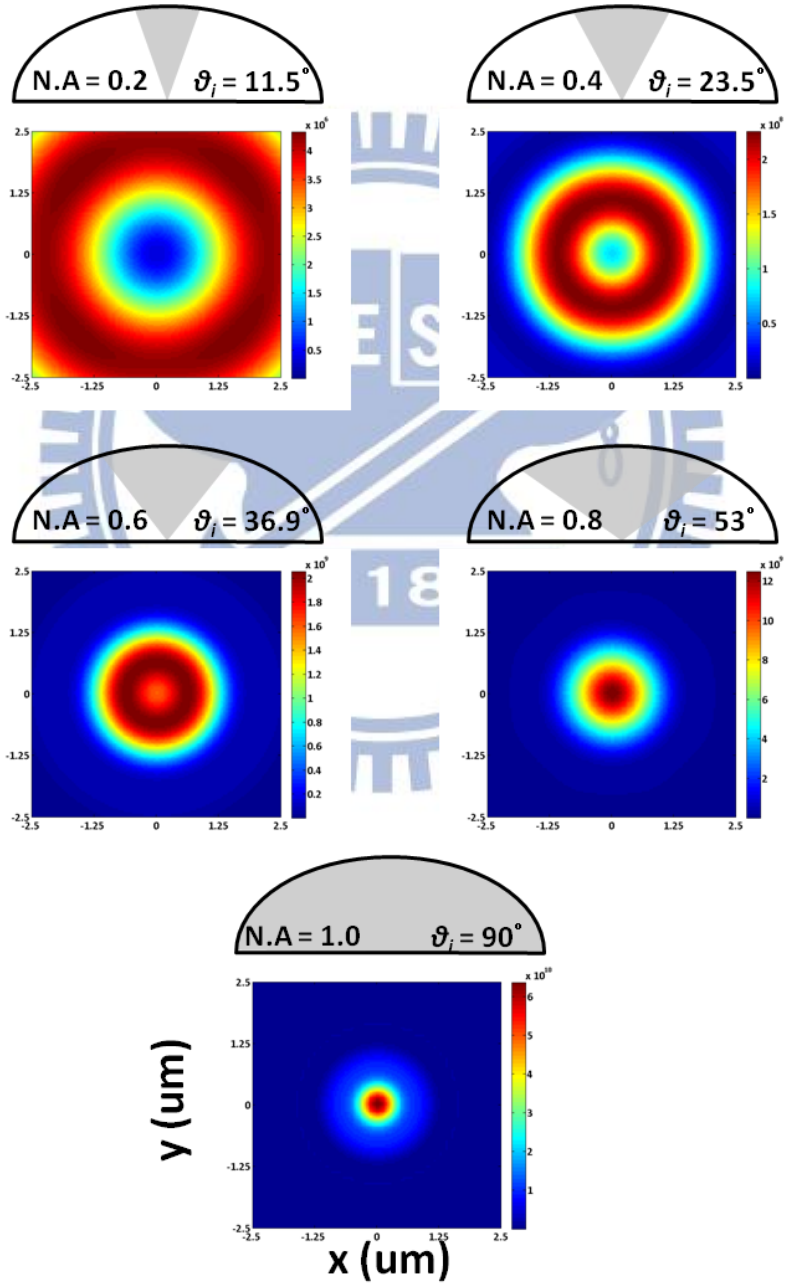

Fig. 3-7 Foci of radial polarization with different N.A

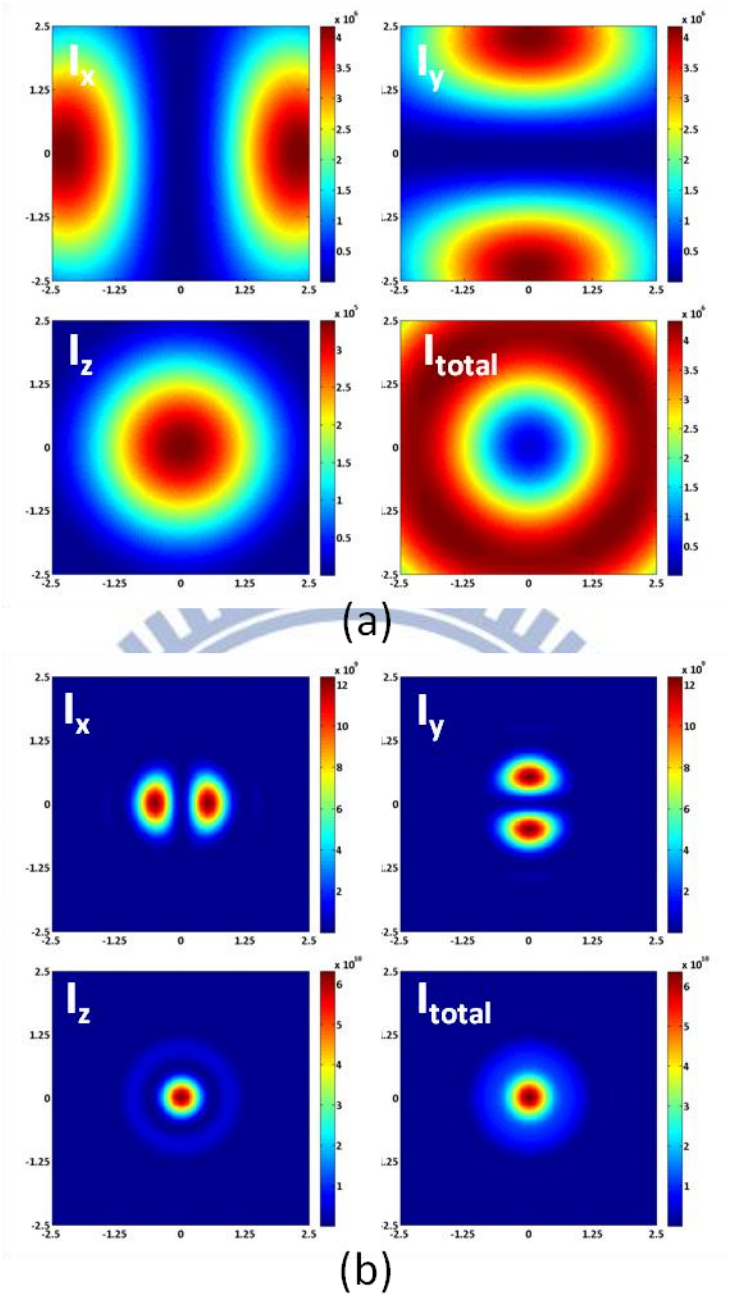

Fig. 3-8 Individual component of foci of radial polarization with (a) N.A = 0.2 (b) 1.0

The total intensity is dominated by transversal component in low N.A system due to the longitudinal component is insignificant. As the N.A increasing, the longitudinal component transcends the other and dominates the total intensity as shown in Fig. 3-8.

3.2.4 Azimuthal polarization

Electric field with vibrated direction along azimuthal direction is called azimuthal polarization. Unlike radial polarization, the *z*-components of one arbitrary point and its symmetrical point at pupil are completely out of phase. This phenomenon results in a completely destructive interference. The total intensity will be a doughnut-shaped distribution due to there is no longitudinal intensity as shown in the following figure.

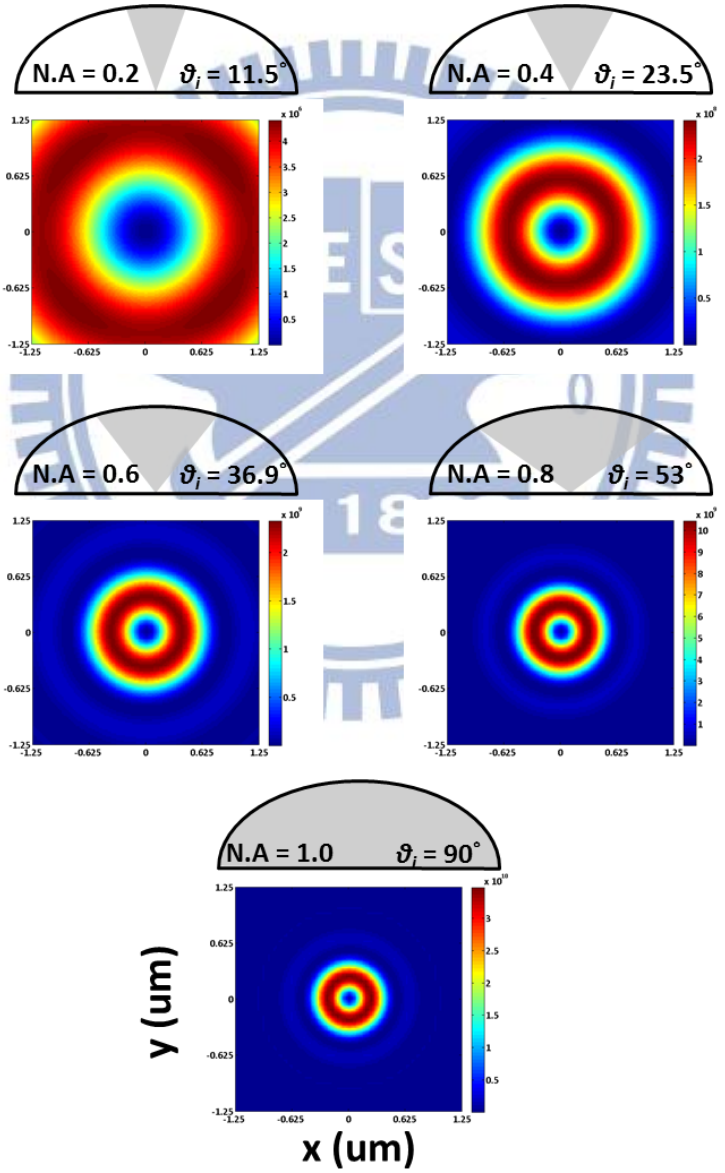

Fig. 3-9 Foci of azimuthal polarization with different N.A

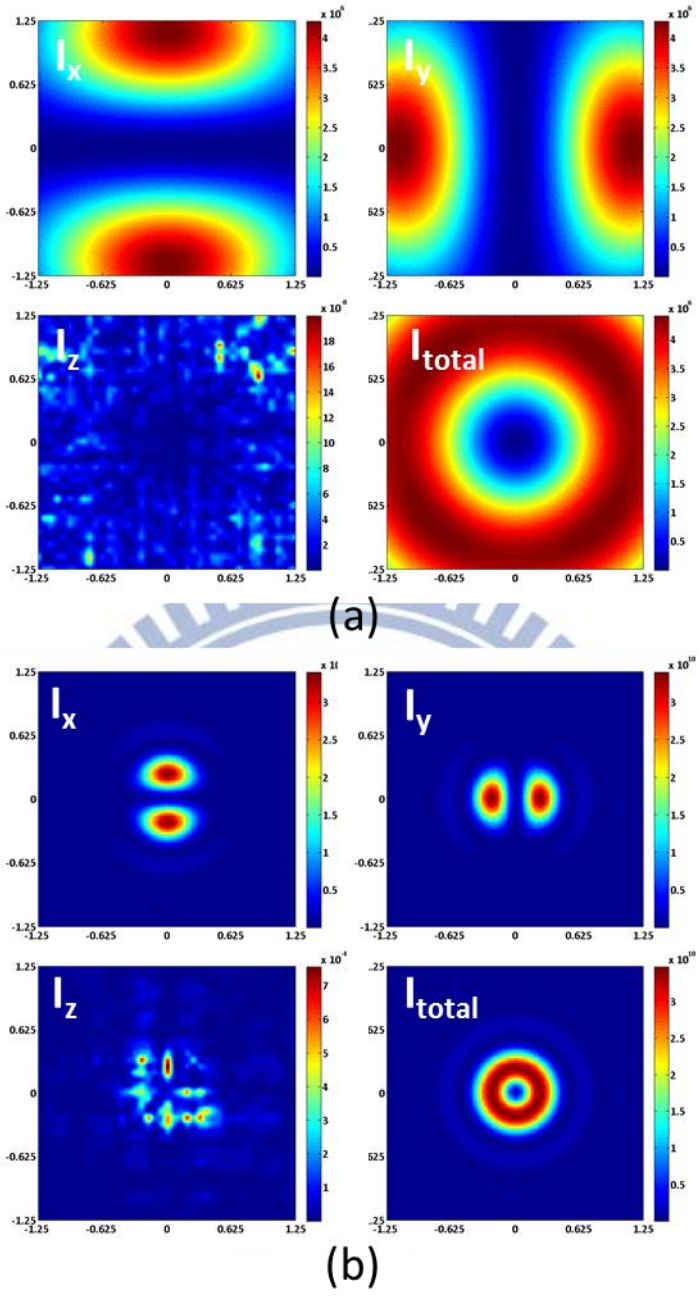

Fig. 3-10Individual component of foci of azimuthal polarization with (a) N.A = 0.2 (b) 1.0

Fig. 3-10 shows the individual intensity of azimuthal polarization. Compared to the transversal intensity, the longitudinal intensity is insignificant even in the high N.A system, resulting in a doughnut-shaped focus.

3.3 Summary

We reviewed different polarizations in this chapter. All of that has its individual characteristic. When the incident beam is linear polarization, there is a “squeezing” effect in the high N.A system. This effect leads to asymmetric focus and is not suitable for some applications. Such effect is not found in circular polarization due to the neutralization of transversal components. However, the focal spot is still too large to modern technology. Fortunately, one of inhomogeneous polarization can provide a small focus by a strongly constructive interference in longitudinal component. The following chapter will use this kind of polarization to a specific application.

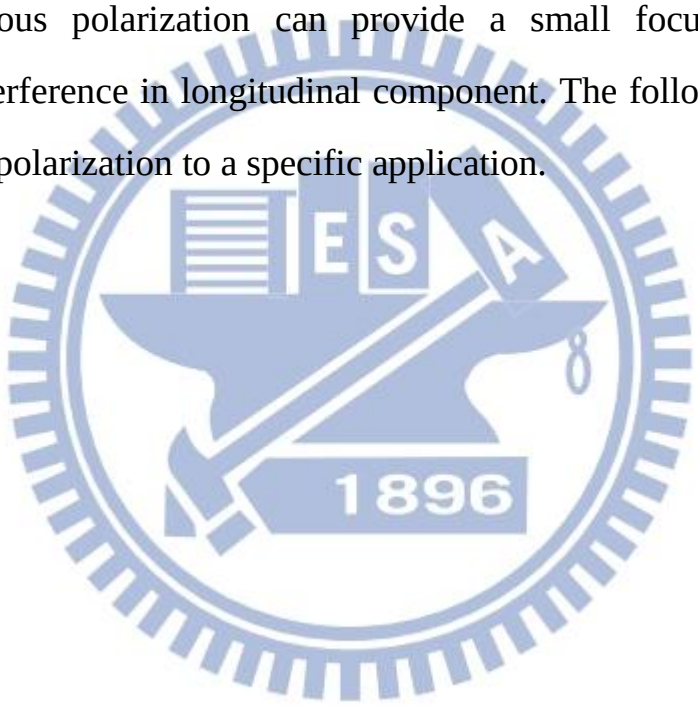

Chapter 4
Surface Plasmon Resonance Sensor

Due to pursuing tiny area and super resolution in modern technology, scientists and engineers try to overcome the natural barrier –"Diffraction limit". Typically, the diffraction limit can be given by $\frac{\lambda}{2NA}$ in transversal direction and half of the coherence length in longitudinal direction [15].By applying the immersion system and shorter wavelength, the transversal resolution can be increased due to larger N.A. The transversal resolution can be further increased by applying inhomogeneous polarized beam. However, the longitudinal resolution of common system is usually several micrometers. In order to detect smaller area in longitudinal direction, in particular, Surface Plasmon Resonance (SPR) is used to analyze the information which is close to the surface region (in dozens of nanometer). In this chapter, we will introduce the principle of SPR and its applications in recent years. Then we will propose two elements to further enhance the performance of SPR sensor.

4.1 Introduction

In 1902, R. W. Wood firstly observed an uncommon phenomenon which did not obey the diffraction theory of grating when a polarized light upright to the groove of metal grating [16]. He attempted to interpret this interesting phenomenon by oscillation with specific polarization of light and metal grating structure. Until 1941, Fano proposed a new opinion that a new electromagnetic wave along the surface when the polarization of light with electric field upright

to the groove of metal grating to define this weird phenomenon [17]. Afterward, this weird electromagnetic wave in the interface was so-called Surface Plasmon Resonance (SPR). After several decades, R. H. Ritchie and R. A. Ferrell *et al* proposed the theoretic model of SPR sequentially [18, 19]. More attention invested in the study of SPR in that it elicited the interests of scientist.

The SPR are collective oscillations of free electrons that can propagate between the metal and dielectric surface. It is a kind of electromagnetic wave which is confined with the sub-wavelength region of surface. As above said, we can find the condition of existence of SPR from Maxwell's equations due to SPR are electromagnetic wave. In order to characterize the properties of SPR, we consider a metal-insulator interface and look for a homogeneous solution of Maxwell's equations with *s*- and *p*-polarization at the surface as shown in Fig. 4-1 [20].

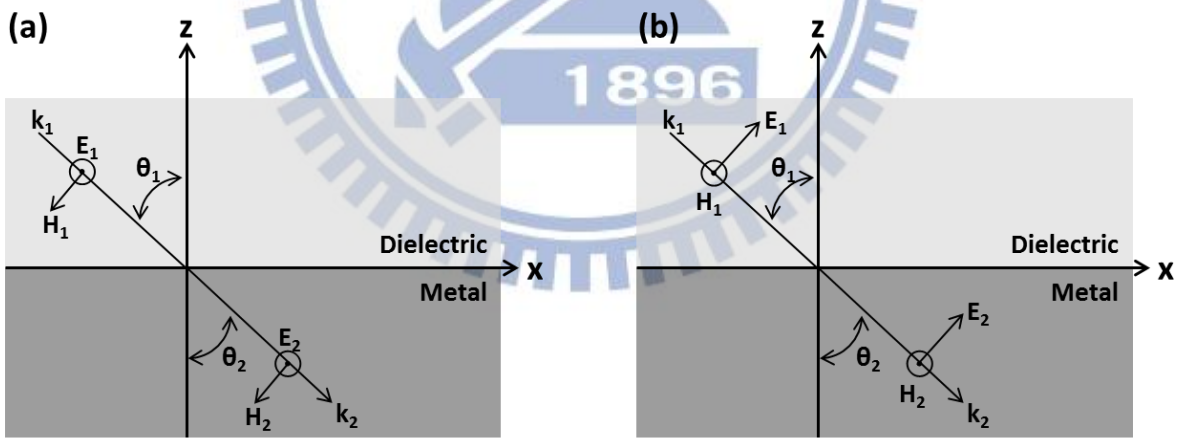

Fig. 4-1Schematic diagram of incident (a) s- (b) p-polarization waves

For *s*-polarization wave, the field at $z > 0$is

$$\vec{H}_1 = \left(H_{1x,}0, H_{1z,}\right)\exp[j(k_{1x}x + k_{1z}z)] \quad (4.1a),$$

$$\vec{E}_1 = \left(0, E_{1y}, 0\right)\exp[j(k_{1x}x + k_{1z}z)] \quad (4.1b)$$

and the field at $z < 0$ is

$$\vec{H}_2 = \left(H_{2x,}0, H_{2z,}\right)\exp[j(k_{2x}x - k_{2z}z)] \quad (4.1c),$$

$$\vec{E}_2 = \left(0, E_{2y}, 0\right)\exp[j(k_{2x}x - k_{2z}z)] \quad (4.1d)$$

respectively. According to the boundary conditions of electromagnetic wave, the continuity of tangential component E_y and H_x lead to the condition

$$k_{1x} = k_{2x} \quad (4.2a),$$

$$k_{1z} + k_{2z} = 0 \quad (4.2b)$$

for nonmagnetic materials. The dispersion relation tell us

$$k_x^2 + k_z^2 = \epsilon\left(\frac{\omega}{c}\right)^2 \quad (4.3).$$

Comparing with Eq. (4.2a) and Eq. (4.2b), the only solution of this equation is $\epsilon_1 = \epsilon_2$ which is contradiction. Hence, there is no surface wave at the interface for *s*-polarization. In other words, the SPR cannot be excited by the *s*-polarized incident wave.

Now we consider the same condition but *p*-polarized incident wave as shown in Fig. 4-1(b). The field at $z > 0$ is

$$\vec{H}_1 = \left(0, H_{1y,}, 0\right)\exp[j(k_{1x}x + k_{1z}z)] \quad (4.4a),$$

$$\vec{E}_1 = (E_{1x}, 0, E_{1z})\exp[j(k_{1x}x + k_{1z}z)] \quad (4.4b)$$

and the field at $z < 0$ is

$$\vec{H}_2 = \left(0, H_{2y,}, 0\right)\exp[j(k_{2x}x - k_{2z}z)] \quad (4.4c),$$

$$\vec{E}_2 = (E_{2x}, 0, E_{2z})\exp[j(k_{2x}x + k_{2z}z)] \quad (4.4d)$$

respectively. Again, the continuity of tangential field results in

$$k_{1x} = k_{2x} \quad (4.5a),$$

$$\frac{k_{2z}}{k_{1z}} = -\frac{\epsilon_2}{\epsilon_1} \quad (4.5b).$$

Combining Eq. (4.5a), Eq. (4.5b) and Eq. (4.3), we arrive at the central result of this section, the dispersion relation of SPR at the interface

$$k_x = k_0\sqrt{\frac{\epsilon_1\epsilon_2}{\epsilon_1+\epsilon_2}} \qquad (4.6).$$

This result shows that there is opportunity to excite the SPR when the incident wave is *p*-polarization. In order to excite the SPR, the permittivity of both media must satisfy the following constraint

$$\epsilon_1 + \epsilon_2 < 0 \qquad (4.7a),$$

$$\epsilon_1\epsilon_2 < 0 \qquad (4.7b)$$

which means that not only either permittivity of two media must be negative but also the absolute value exceeding the other. Most of metals, in particular, noble metals have large negative real part of dielectric constant. Therefore, the SPR can exist at the interface between noble metal and dielectric when the incident wave is *p*-polarization.

However, the SPR cannot be excited by common methods due to the wavevector of SPR k_{SP} is always larger than incident wavevector in dielectric k_{1x} as shown in Fig. 4-2.

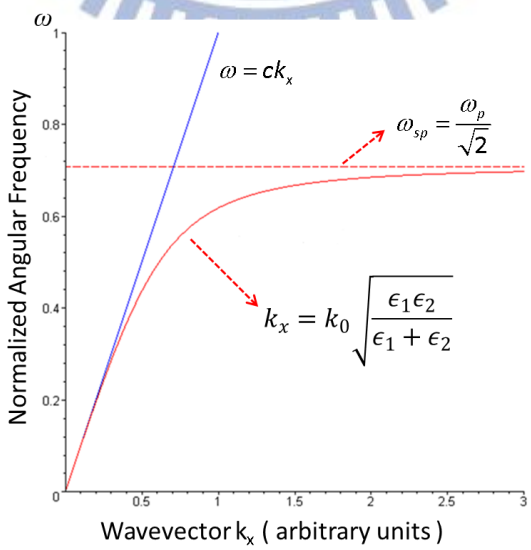

Fig. 4-2 Dispersion relations of SPR and dielectric

The mechanism of Surface Plasmon Polaritons (SPPs) excitation was generally induced by a prism-based coupler, firstly proposed by Kretschmann and Otto in 1968[21, 22].Due to the difficulty of fabrication, Kretschmann's configuration was more acceptable than the others. Figure 4-3 shows Kretschmann's configuration and its dispersion relations.

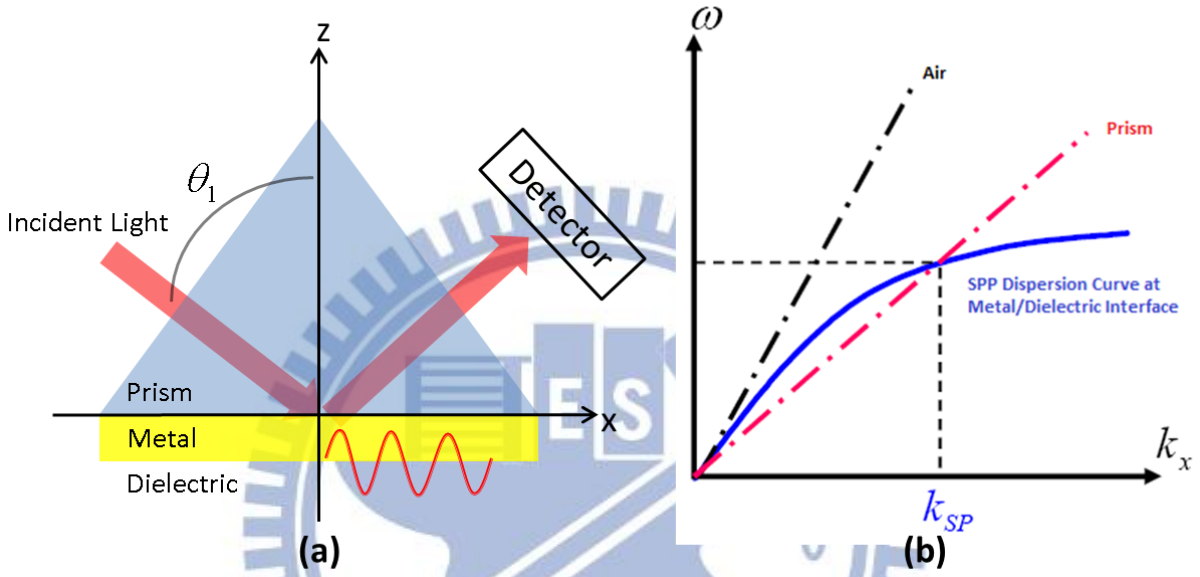

Fig. 4-3 (a) Kretschmann's configuration and (b) its dispersion relations

The phase matching condition in this system is

$$k_{1x} = n_1 k_0 \sin\theta_1 = k_{SP} = k_0 \sqrt{\frac{\epsilon_1 \epsilon_2}{\epsilon_1 + \epsilon_2}} \qquad (4.8)$$

at the intersection point in Fig. 4-3b. By applying angular scanning, we can observe a diagram of the reflectance vs. incident angle as shown in Fig. 4-4.The peak of this curve refers to the total-internal reflection and the dip relates to the incident light to be coupled to the SPR.Although Kretschmann's configuration can provide us polychromatic information, it remains a problem that the measurement needs angle scanning which may lead to a time consuming issue.

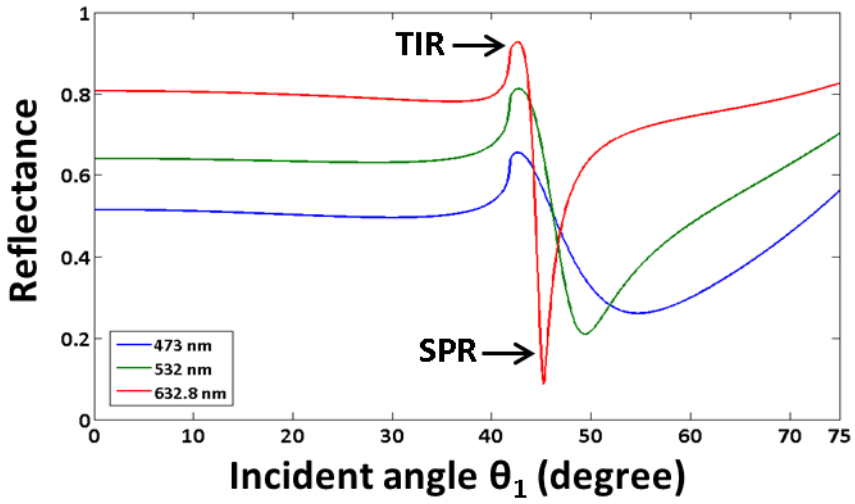

Fig. 4-4 Angular reflectance of Kretschmann's configuration

In order to solve this issue, H. Kano then replaced the prism by a collinear objective lens to enable a universal wavevector without the need for angular scanning after several decades[23].Due to the intrinsic characterization of SPR, the incident polarization of Kano's configuration must be radial polarization and the N.A of objective lens must be as higher as possible. The phase matching condition and the configuration are shown as follower.

$$k_{1x} = n_1 k_0 \sin\theta_{SP} = (N.A)k_0 = k_{SP} \qquad (4.9)$$

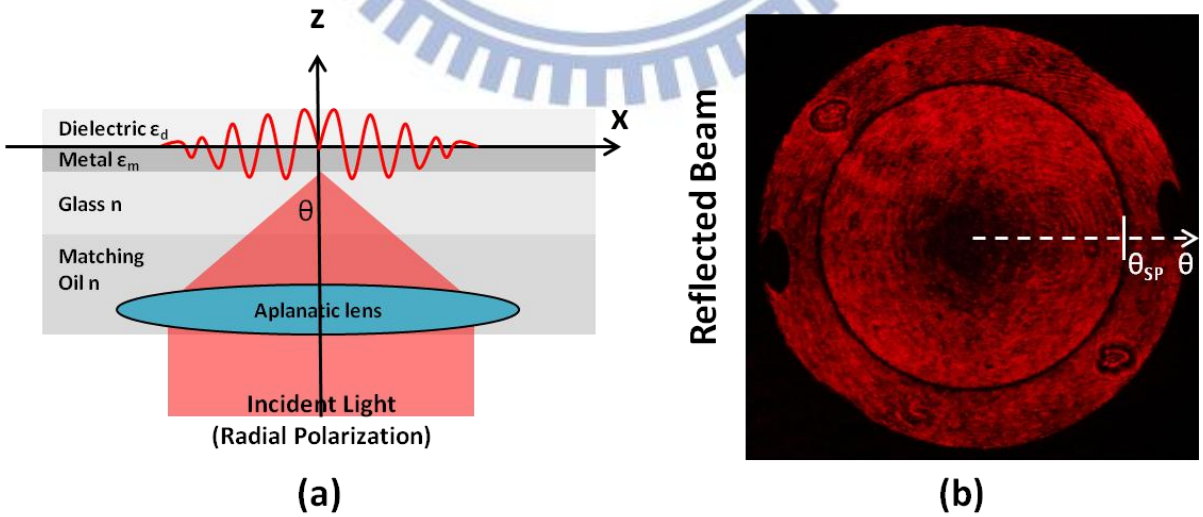

Fig. 4-5 (a) Kano's configuration and (b) reflected beam

This configuration combining the advantages of radial polarization and SPR, not only provides a super transversal resolution but also in longitudinal. The necessity of relying wavelength-dependent optical elements to generate radially polarized light has been widely used on RP-SPR sensor [24-32]. However, there are two issues should be considered. Firstly, to our knowledge, there is no synthesized method has been published to generate a polychromatic radial polarization. Besides, the numerical aperture of objective lens limits the maximum incident angle so that we cannot excite surface plasma which requires larger wavenumber.

In this chapter, we propose two elements to improve the performance of objective-based SPR sensor, integrating a polychromatic objective-based SPR sensor with larger sensing range.

4.2 Experimental setup

The experimental setup of proposed polychromatic SPR sensor can be divided into two major parts. The first part deals with the synthesis of polychromatic radial polarization via a Spatially Varying Polarizer (SVP); the second part is a Metal-Insulator-Metal (MIM) coupler for extending sensing range of this system as shown in the Fig. 4-6. A white light LED module (Luxeon Star/O LXHL-NWE8) is utilized as a light source which is collimated by the collimated lens (CL). The unpolarized white light is converted to the radial polarization, and then relays to the entrance pupil of the commercial inverted microscope (Olympus IX-71) with oil-immersion objective lens (Olympus PlanApo-N 60x/1.45 Oil). The N.A of dry lens is about 0.97 and the corresponding half divergence angle is 75.16° which is well beyond the resonant

angle of SPR $\theta_{SP} \approx 43°$ at $\lambda = 632.8$ nm.

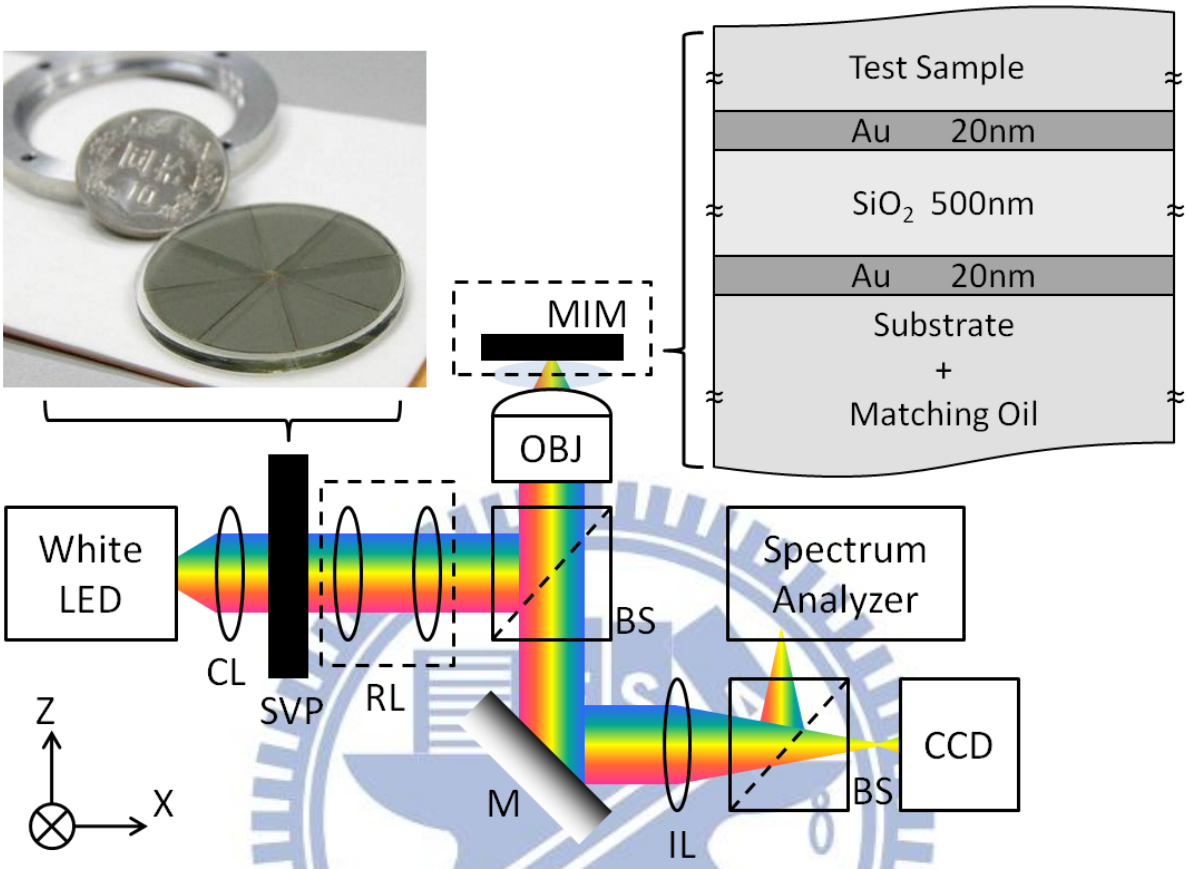

Fig. 4-6 Configuration of the polychromatic SPR sensor, where CL: collimated lens, SVP: spatially varying polarizer, RL: relay lens, BS: beam splitter, M: mirror, IL: image lens, MIM: metal-insulator-metal coupler.

After a strong focusing by the oil-immersion objective lens at the interface between the substrate and metal, waves with specific incident angle couple to the SPR and the others reflect. The reflected beam is collected by the same objective lens and guides backward into two differentoptical paths. One projects the reflected beam onto CCD image sensor from the back focal plane. The other one records the spectrum of reflected beam via a spectrum analyzer (CYT USB-100 MicroSpec).

4.2.1 Chromatically radial polarization

A chromatically spatial inhomogeneous polarization can be generated by a designed Spatially Varying Polarizer (SVP). The spatial varying polarizer can ready produced by n part linear polarizer where the arrow represents the transmitted axis as shown in the Fig. 4-7.

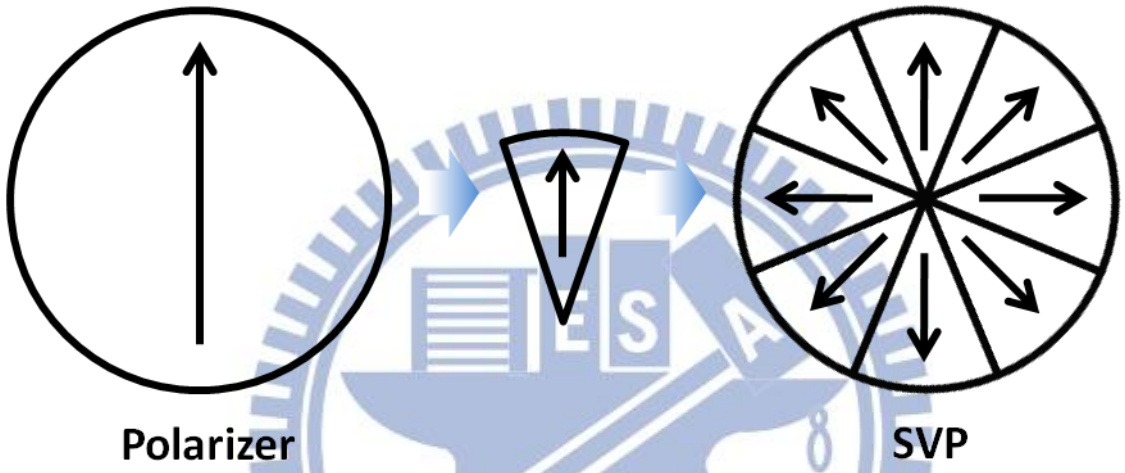

Fig. 4-7 Designed concept of SVP for radial polarization

By combining these n pieces of individual polarizer, a polychromatic radially polarized beam can be generated in a cost-effective way. Based on previous studies, the common recipes of synthesizing or generating radial polarization are designed by elements such as phase plate, liquid crystal, resonant cavity and interference[33-36]. These methods used wavelength dependent elements for a particular working wavelength. On the contrary, proposed SVP is assembled by conventional polarized element which is wavelength independent.

We can use an analyzer to test the performance of our homemade radial polarizer as shown in the following.The following field distribution indeed shows a good result under the tests of different transmitted angle.

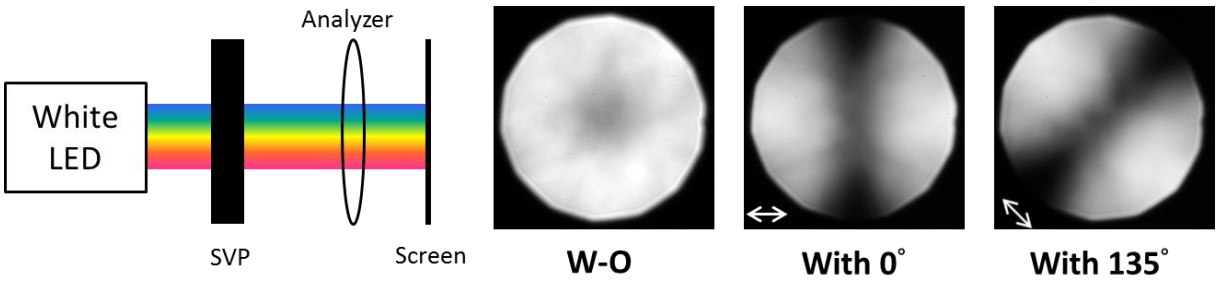

Fig. 4-8 Performance of SVP with different transmitted angle

4.2.2 Metal-insulator-metal coupler

On dealing with second task, we proposed the metal-insulator-metal coupler between the substrate and sample layer as shown in Fig.4-6.This structure was first proposed by D. Liu for generating chromatic SPR in the same time [37] and will be degenerated into Kano's configuration without the insulator layer. The parameters of this MIM coupler are shown in the following table (for working wavelength = 632.8 nm).

	ε	**n**
Au	-9.80+j1.97	
SiO_2		1.5
Substrate		1.5
Matching Oil		1.5

Table 4-1 Parameters of MIM coupler for λ= 632.8 nm

Due to the sandwich structure, the incident wave has potential to induce the cavity resonance (CR) modes just like the Fabry–Pérot resonator. The detail of this modes conversion will be discussed in the next section.

4.3 Simulated and experimental results

The simulated method of multilayer structure is matrix approach which is well used in physical optics. This method is facilitated to track the complex amplitudes of the incident and reflected waves through the boundaries of multilayer structure. Considering we have two waves propagating along both directions of the optical axis, the electric fields can be written as follower

$$E_1 = (A_1 e^{jk_{1x}x} + B_1 e^{-jk_{1x}x}) e^{jk_{1z}z} \quad (4.10a),$$

$$E_2 = (A_2 e^{jk_{2x}x} + B_2 e^{-jk_{2x}x}) e^{jk_{2z}z} \quad (4.10b)$$

where the A_1 and A_2 are the amplitudes of forward-traveling wave along the +z direction, and B_1 and B_2 are the amplitudes of backward-traveling wave along the other direction.

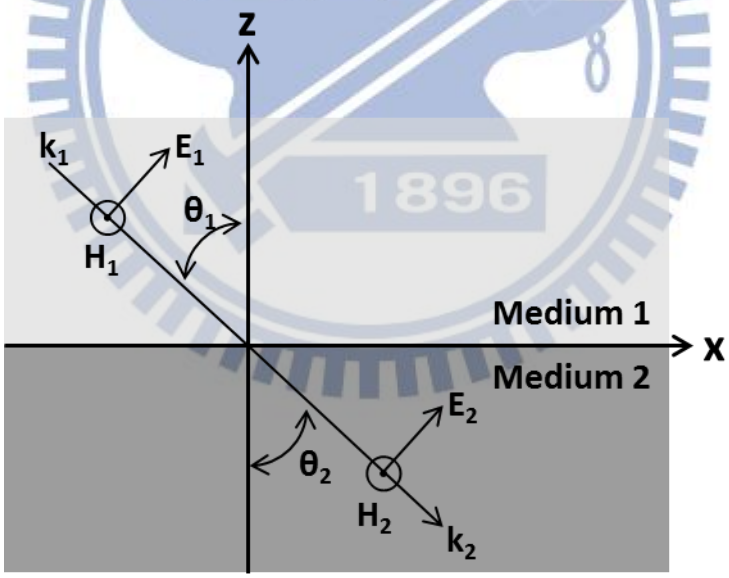

Fig. 4-9 Schematic diagram of transition matrix

The relationship between A_1, A_2, B_1 and B_2 can be obtained by solving the boundary condition

$$\begin{bmatrix} A_1 \\ B_1 \end{bmatrix} = \frac{1}{t_{12}} \begin{bmatrix} 1 & r_{12} \\ r_{12} & 1 \end{bmatrix} \begin{bmatrix} A_2 \\ B_2 \end{bmatrix} = \mathbf{D_{12}} \begin{bmatrix} A_2 \\ B_2 \end{bmatrix} \quad (4.11)$$

where t_{12} and r_{12} are the Fresnel reflection and transmission coefficients,

$\mathbf{D_{12}}$is the transition matrix at the interface of medium 1 and 2 depending on the polarization of waves (in our case is *p*-polarization).

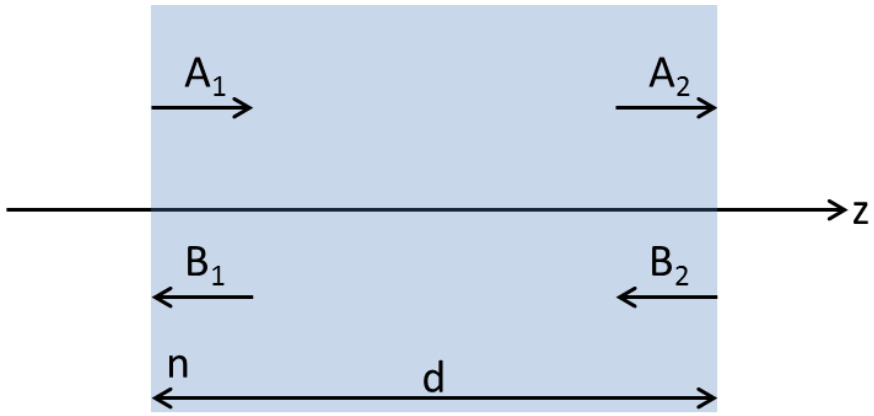

Fig. 4-10 Geometry for propagation matrix

The propagation behavior of waves in homogeneous media with refractive index *n* and thickness *d* can be described as a matrix called propagation matrix

$$\begin{bmatrix} A_2 \\ B_2 \end{bmatrix} = \begin{bmatrix} e^{-jk_z d} & 0 \\ 0 & e^{jk_z d} \end{bmatrix} \begin{bmatrix} A_1 \\ B_1 \end{bmatrix} \Rightarrow \begin{bmatrix} A_1 \\ B_1 \end{bmatrix} = \begin{bmatrix} e^{j\phi} & 0 \\ 0 & e^{-j\phi} \end{bmatrix} \begin{bmatrix} A_2 \\ B_2 \end{bmatrix} = \mathbf{P} \begin{bmatrix} A_2 \\ B_2 \end{bmatrix} \quad (4.12)$$

where $\phi = k_z d = n d k_0 \cos\theta$ ($\cos\theta$ for oblique incident wave) and $\mathbf{P}$ is the propagation matrix.

Combining the transition and propagation matrix, we can describe waves in the multilayer structure. For example, a n-layer structure system which is shown in Fig. 4-11 can be simply related to the following equation.

$$\begin{aligned} \begin{bmatrix} A_0 \\ B_0 \end{bmatrix} &= \mathbf{D_0^{-1}}\left(\mathbf{D_1 P_1 D_1^{-1}}\right)\left(\mathbf{D_2 P_2 D_2^{-1}}\right)\cdots\left(\mathbf{D_{N-1} P_{N-1} D_{N-1}^{-1}}\right)\mathbf{D_N} \begin{bmatrix} A_N \\ B_N \end{bmatrix} \\ &= \begin{bmatrix} M_{11} & M_{12} \\ M_{21} & M_{22} \end{bmatrix} \begin{bmatrix} A_N \\ B_N \end{bmatrix} = \mathbf{M} \begin{bmatrix} A_N \\ B_N \end{bmatrix} \end{aligned} \quad (4.13)$$

where $\mathbf{M}$is the transfer matrix of this multilayer system. Typically, $B_N = 0$ due to there is no wave propagating form the last layer. Therefore, the Fresnel coefficient can be calculated by an intrinsic relation

$$A_0 = M_{11} A_N \quad (4.14a),$$

$$B_0 = M_{21} A_N \quad (4.14b)$$

and we have Fresnel coefficient

$$t = \frac{A_N}{A_0} = \frac{1}{M_{11}} \quad (4.15a),$$

$$r = \frac{B_0}{A_0} = \frac{M_{21}}{M_{11}} \quad (4.15b).$$

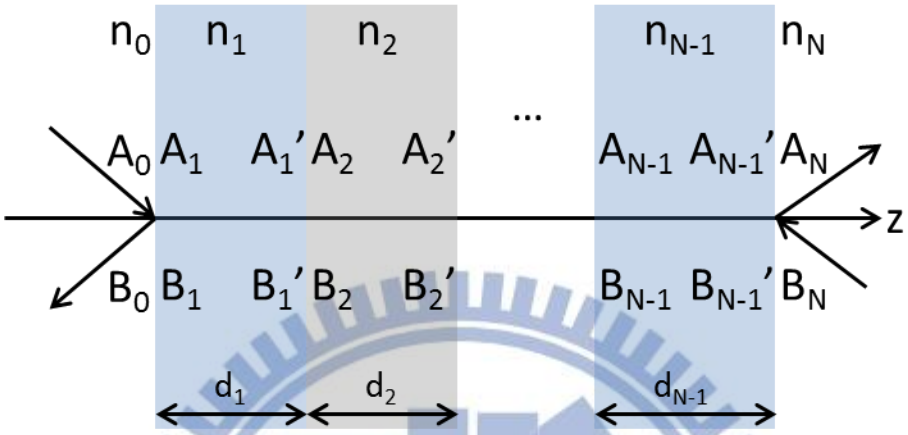

Fig. 4-11 Matrix approach of multilayer structure

The following section will simulate the MIM structure based on this result.

4.3.1 Discussions

We first consider the condition with the 20 nm Au / d nm SiO_2 / 20 nm Au and the parameters are same as shown in table 4-1. The working wavelength is 632.8 nm. When we increase the thickness of insulator layer, the cavity resonance modes at small incident angle are induced by a Fabry-Perot-liked resonator as shown in Fig. 4-12. The CR modes at large angle are likely to be coupled into another mode.

For clarifying the characteristic of these two modes, we change refractive index of the sample n as shown in Fig. 4-13. The result shows that only the transmitted mode has response to the change on dielectric. This phenomenon

proves that the transmitted mode is SPR which might be used to extend sensing range.

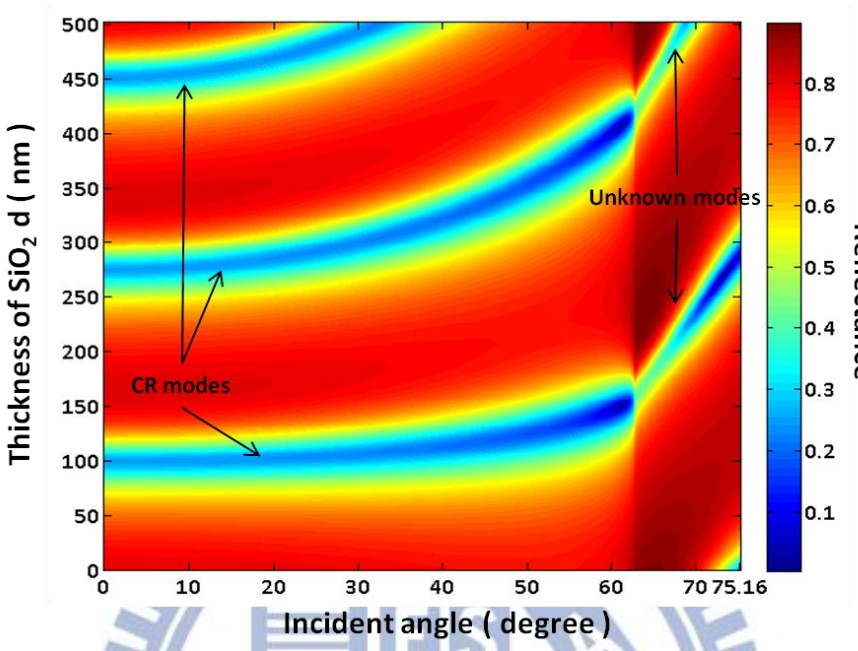

Fig. 4-12 Reflectance vs. different incident angle and thickness of SiO_2 d for λ=632.8 nm

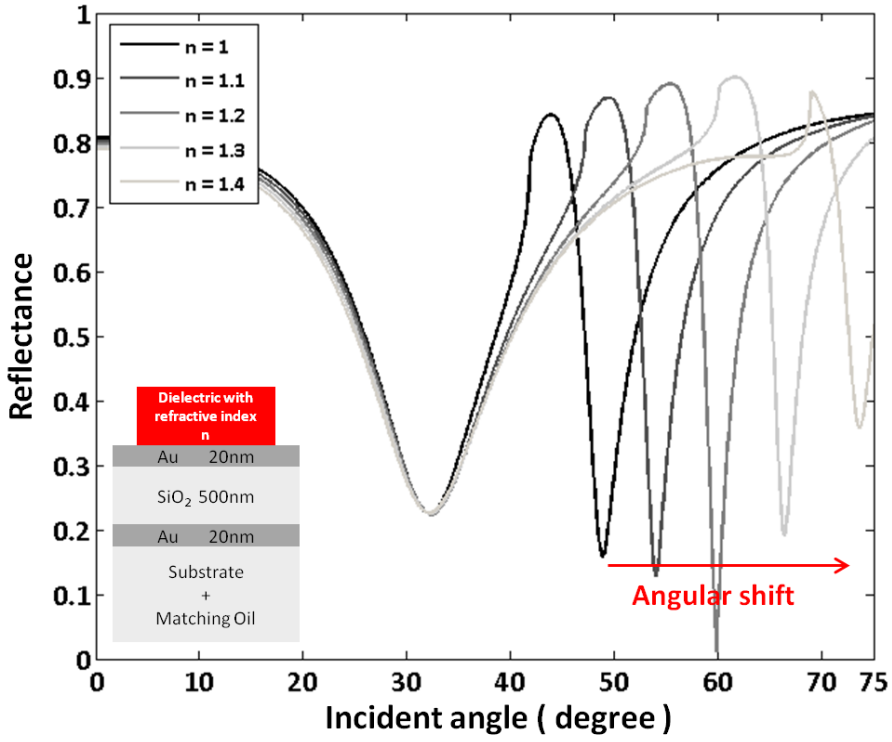

Fig. 4-13 Reflectance vs. sample with different refractive index

The transmitted SPR mode is induced by the CR mode due to the interference inside sandwich structure likely provides a secondary light source with larger wavevector.

In order to further discuss the enhancement of sensing range, we compare the proposed SPR sensor with traditional SPR sensor as shown in the following.

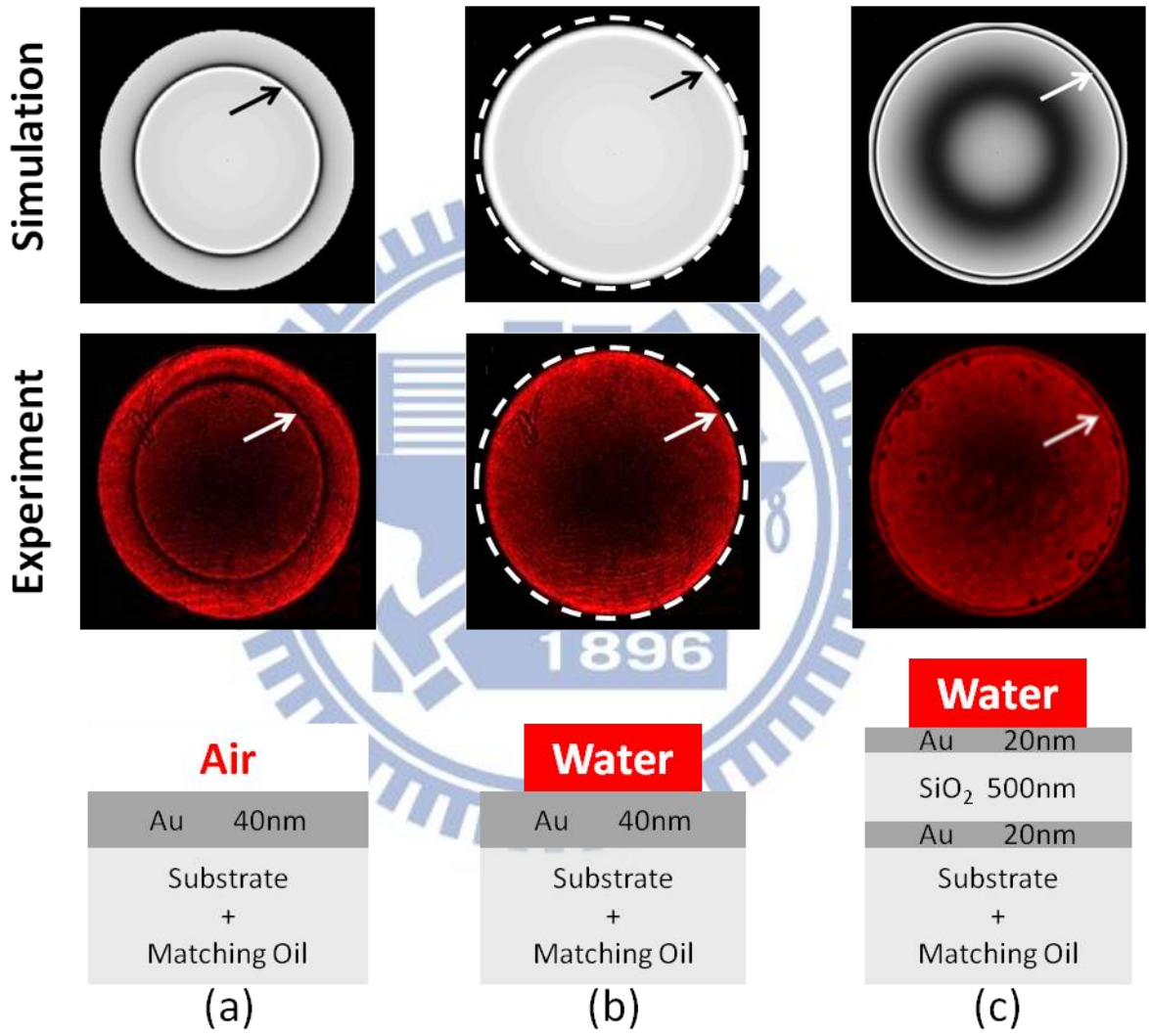

Fig. 4-14 Traditional SPR sensor with (a) air and (b) water, (c) proposed SPR sensor with water

Fig. 4-14(a) shows the traditional structure with air. The resonant dark ring is within the maximum divergence angle of the objective lens. The following shows the same structure but with water. The dark ring exceeds the

divergence angle of objective so that we cannot observe it. Finally we show the MIM coupler with water. We can see the dark ring would be mapped within the back aperture is pulled back to the viewing angle. By simulation, the maximum refractive index we can observe in this structure is about 1.42. The sensing range is improvedby the MIM coupler about 11%.

After discussing the behavior and the performance of MIM coupler, we change the condition to the different incident wavelength with thickness = 500 nm. The following figure shows only long wavelength can couple to the SPR in the conventional structure. However, the proposed coupler can generate SPR with different wavelength in the same incident angle.

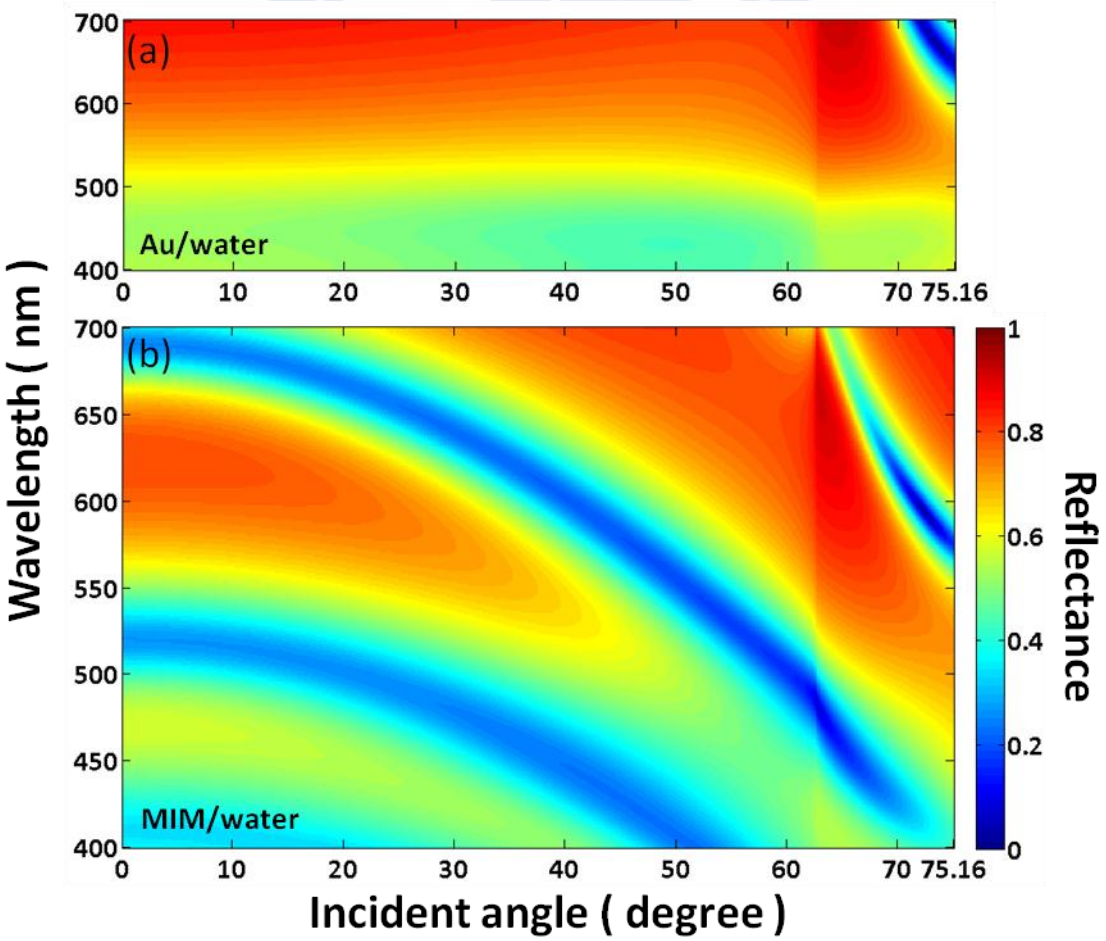

Fig. 4-15 Reflectance vs. wavelength and incident angle for (a) traditional coupler and (b) MIM coupler

Finally, we integrate the SVP and the MIM coupler, a polychromatic SPR is excited and the reflected beam is imaged by the CCD as shown in the following figure.

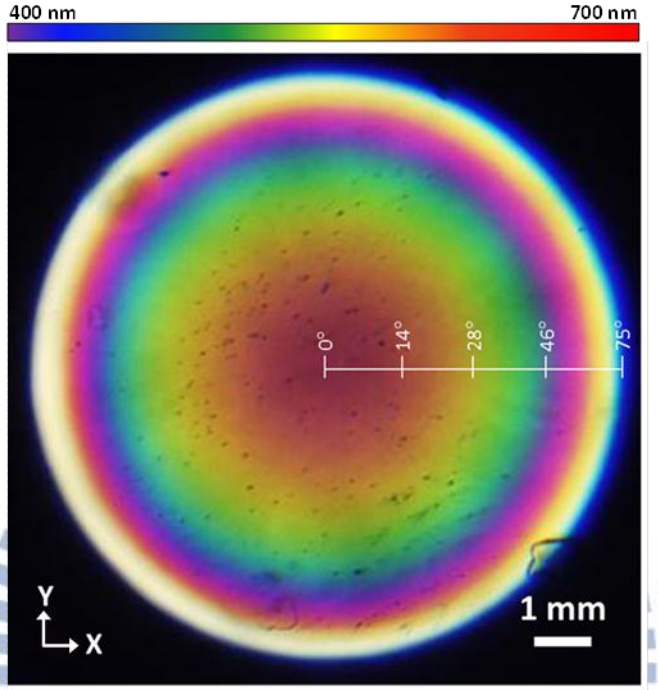

Fig. 4-16 Field distribution of white light radial polarization induces rainbow ring at the exit pupil of objective lens

Up to this point, a system simultaneously capturing the two-dimensional angular/spectral SPR is implemented. We take advantage of highly optical throughput to further pursue a dynamic operation. Equipped with a real-time spectral acquisition system, a proof-of-concept scenario is demonstrated by changing the concentration of a NaCl solution. The variation in concentration will cause dispersive refractive index change, results in fine variations on the color appearance of rainbow rings. The information can be extracted and quantified by integrating the intensity of individual color band via spectrometer. The normalized differential spectral reflectance (DSR) shown in Fig. 4-17 presents the variation of spectral reflectance subject to different concentration of

NaCl solution, ρ = 10%, 20%, 30%, and 40%, respectively, where the reflectance is subtracted by the baseline of pure water.

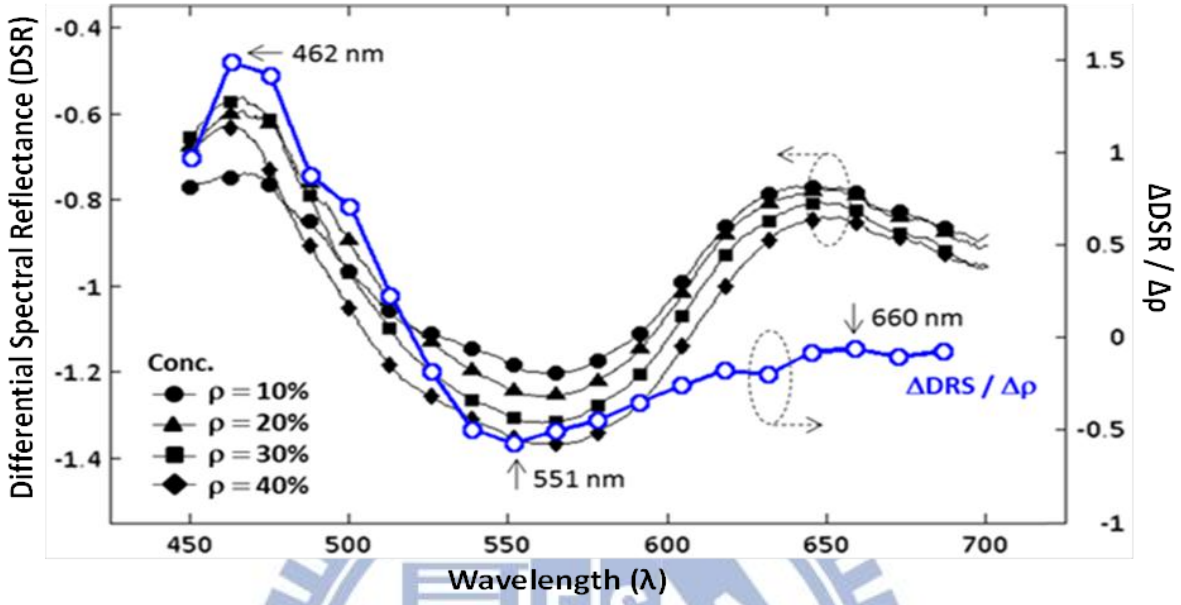

Fig. 4-17 Differential spectral reflectance (DSR) subject to different concentration of NaCl solution, $\rho = 10\%, 20\%, 30\%$ and 40%, respectively, where the reflectance was subtracted by the baseline of pure water. As we difference the variation of spectral reflectance with respect to concentration change ($\Delta\rho = 10\% - 20\%$), $\Delta DSR/\Delta\rho$, three peaked wavelengths (462 nm, 551 nm, and 660 nm) are highlighted to feature the most sensitive spectral response

The differential signal can be treated as the observation windows for monitoring the concentration change of a salt solution in real time. We expect the proposed scenario to be a useful reference for researchers to highlight or differentiate some unknown bio-chemical features, which suffers from inefficiency and time consuming in transitional sensor.

4.4 Summary

In the beginning of this chapter, we first introduce the developments of surface plasmon resonance (SPR). Then we applied spatially inhomogeneous polarization beam to a specific application, which can observe area beyond the diffraction limit in both transversal and longitudinal direction. Afterward, such SPR sensor was improved by the proposed elements. The spatially varying polarizer (SVP) generated chromatically radial polarization and metal-insulator-metal (MIM) coupler extended the sensing range of refractive index. Finally, a rainbow ring was obtained and utilized to monitor the concentration change of test sample.

Chapter 5
Conclusions and Future Works

5.1 Conclusions

In this thesis, we clarified the concept of vector diffraction theory and illustrated the focal field distribution of polarization by the vector point spread function (VPSF). Different pupil mask were introduced in the chapter 2. Then we kept our attention on the polarization mask and demonstrated that different polarization fields would distort in high N.A system due to the components in low N.A system were negligible but should be considered in high N.A system. Besides, the inhomogeneous polarization in high N.A system showed a potential for super resolution in that the strong focus of the longitudinal component.

In order to extract the information in a sub-wavelength region, we applied the spatially inhomogeneous polarization to surface plasmon resonance (SPR) sensor. Afterward, a chromatically radial polarization was synthesized by spatially varying polarizer (SVP) and the sensing range was extended about 11% ($n = 1.28 \rightarrow 1.42$) by the metal-insulator-metal (MIM) coupler. In the end of this thesis, a proof-of-concept scenario was demonstrated by changing the concentration of a NaCl solution. Preliminary outcome was published in the literature [38, 39]. We expect to apply related technology to nanotechnology in the future.

5.2 Future work

So far, we already confirm the performance of proposed SPR sensor. The

unique rainbow concentric ring involves very rich information about the sub-wavelength region. A two-dimensional spectral image of SPR can be extracted if we integrate this SPR sensor system with a moving stage. This idea is illustrated by Fig. 5-1.

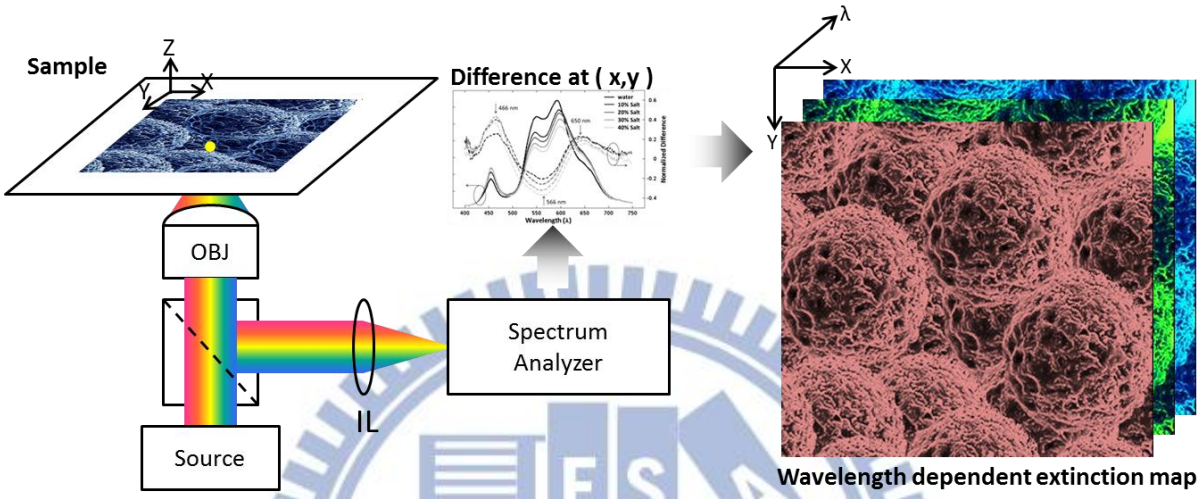

Fig. 5-1 Schematic diagram of SPR spectral imaging system

However, the oil-immersion objective lens not only provides a high N.A system and the phase matching condition but also a shallow depth of focus. This intrinsic characterization leads to a sensitive focus. Moreover, as we scanning, the oil between the objective lens and the substrate will play an important role due to the viscosity of oil will affect the focus. The SPR spectral image will bring a great impact to novel technology if the defocus issue can be solved.

Another interesting phenomenon was observed during our research. A sparse particle at the near field region around the focus would induce some weird interference patterns at the far field as shown in Fig. 5-2. That means we can extract or reconstruct some near-field information from the far-field image. Novel technologies need point-by-point scanning to achieve superresolution imaging which may leads to a time-consuming issue. In order to solve this issue, we replace the incident lens with a lens array. These lenses will excite SPR at

different position and collect the reflected images at once. Due to the dimension of the lens array, this method may reduce the resolution of our system. However, by analyzing different snap-shot images with different conditions, we may reconstruct the near-field image with high resolution by the technique of Compressive Sensing (CS). We think this method can provide a real-time image and extend the effective field of view of the next generation microscopy.

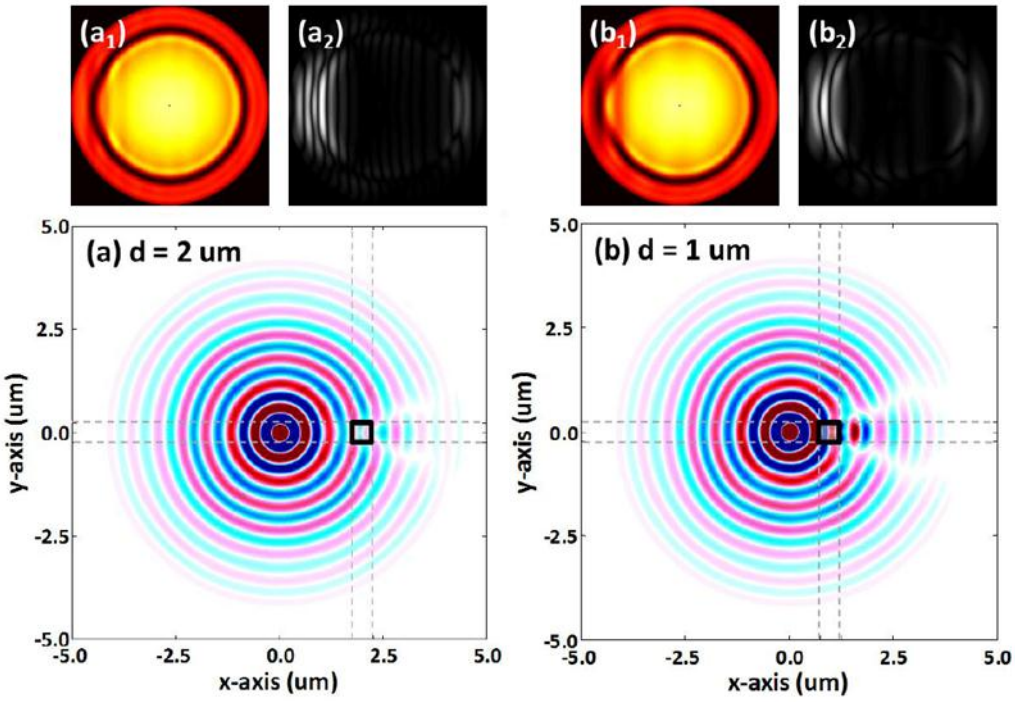

Fig. 5-2 Sparse particle induces interference pattern at the far field

References

[1] J. W. Goodman, *Introduction to Fourier Optics* (McGraw-Hill, New York, 1968).

[2] M. Born and E. Wolf, *Principles of Optics 7th ed.* (University Press, Cambridge, 2005).

[3] W. Singer, M. Totzeck and H. Gross, *Handbook of Optical Systems Vol. 2* (Wiley-VCH Verlag, Weinheim, 2005).

[4] M. E. Testorf, B. M. Hennelly and J. Ojeda-Castañeda, *Phase-Space Optics Fundamentals and Applications* (McGraw-Hill, New York, 2010).

[5] W. Mecklenbräuker and F. Hlawatsch, *The Wigner Distribution* (Elsevier, Amsterdam, 1997).

[6] M. A. Alonso, "Wigner functions in optics: describing beams as ray bundles and pulses as particle ensembles," Adv. Opt. Photon. **3**, 272-365 (2011).

[7] R. L. Easton, Jr. Fourier Methods in Imaging (John Wiley & Sons Ltd, UK 2010).

[8] E. R. Dowski, Jr. and W. T. Cathey, "Extend depth of field through wave-front coding," Appl. Opt. **11**, 1859-1866 (1995).

[9] A. A. Tovar, "Production and propagation of cylindrically polarized Laguerre-Gaussian laser beams," Journal of the Optical Society of America a-Optics Image Science and Vision **15**, 2705-2711 (1998).

[10] I. Moshe, S. Jackel and A. Meir, "Production of radially or azimuthally polarized beams in solid-state lasers and the elimination of thermally induced birefringence effects," Opt. Lett. **28**, 807-809 (2003).

[11] R. Dorn, S. Quabis, and G. Leuchs, "Sharper focus for a radially polarized light beam," Phys. Rev. Lett. **91** (2003).

[12] G. Machavariani, Y. Lumer, I. Moshe, A. Meir and S. Jacket, "Efficient extracavity generation of radially and azimuthally polarized beams," Opt. Lett. **32**, 1468-1470 (2007).

[13] H. W. Ren, Y. H. Lin and S. T. Wu, "Linear to axial or radial polarization

conversion using a liquid crystal gel," Appl. Phys. Lett. **89**, 3 (2006).

[14] T. H. Lan and C. H. Tien, "Study on focusing mechanism of radial polarization with immersion objective,"Jpn. J. Appl. Phys. **47**, 5806-5808 (2008).

[15] C. Akcay, P. Parrein and J. P. Rolland, "Estimation of longitudinal resolution in optical coherence imaging," Appl. Opt. **25**, 5256-5262 (2002).

[16] R. W. Wood, "On a remarkable case of uneven distribution of light in a diffraction grating spectrum," Philos. Mag. **4**, 396-402 (1902).

[17] U. Fano, "The theory of anomalous diffraction gratings and quasi-stationary waves on metallic surfaces," J. Opt. Soc. Am. **31**, 213-222 (1941).

[18] R. H. Ritchie, "Plasma losses by fast electrons in thin films," Phys. Rev. **106**, 874-881 (1957).

[19] E. A. Stern and R. A. Ferrell, "Surface plasma oscillations of a degenerate electron gas," Phys. Rev. **120**, 130-136 (1960).

[20] S. A. Maier, *Plasmonics: Fundamentals and Applications* (Springer, UK, 2006).

[21] E. Kretschmann and H. Raether, "Radiative decay of non-radiative surface plasmons excited by light," Zei. Phys. A **23**, 2135 (1968).

[22] A. Otto, "Excitation of nonradiative surface plasma waves in silver method of frustrated total reflection,"Zei. Phys. **216**, 398 (1968).

[23] H. Kano and W. Knoll, "Locally excited surface plasmon polaritons for thickness measurement of LBK films," Opt. Commun. **153**, 235 (1998).

[24] K. J. Moh, X. C. Yuan, J. Bu, S. W. Zhu and B. Z. Gao, "Surface plasmon resonance imaging of cell-substrate contacts with radially polarized beams," Opt. Express **16**, 20734-20741 (2008).

[25] R. Vander and S. G. Lipson, "High-resolution surface-plasmon resonance real-time imaging," Opt. Lett. **34**, 37-39 (2009).

[26] Q. W. Zhan, "Evanescent Bessel beam generation via surface plasmon resonance excitation by a radially polarized beam," Opt. Lett. 31,

1726-1728 (2006).

[27] W. B. Chen and Q. W. Zhan, “Realization of an evanescent Bessel beam via surface plasmon interference excited by a radially polarized beam,” Opt. Lett. **34**, 722-724 (2009).

[28] M. G. Somekh, G. Stabler, S. G. Liu, J. Zhang and C. W. See, “Wide-field high-resolution surface-plasmon interference microscopy,” Opt. Lett. **34**, 3110-3112 (2009).

[29] K. A. Willets and R. P. Van Duyne, “Localized surface plasmon resonance spectroscopy and sensing,” Annu. Rev. Phys. Chem. **58**, 267-297 (2007).

[30] A. Duval, A. Laisne, D. Pompon, S. Held, A. Bellemain, J. Moreau and M. Canva, “Polarimetric surface plasmon resonance imaging biosensor,” Opt. Lett. **34**, 3634-3636 (2009).

[31] K. J. Moh, X. C. Yuan, J. Bu, S. W. Zhu and B. Z. Gao, “Radial polarization induced surface plasmon virtual probe for two-photon fluorescence microscopy,” Opt. Lett. **34**, 971-973 (2009).

[32] J, Homola, “Surface plasmon resonance sensors for detection of chemical and biological species,” Chem. Rev. **108**, 462-493 (2008).

[33] G. Machavariani, Y. Lumer, I. Moshe, A. Meir and S. Jackel, “Effiecient extracavity generation of radially and azimuthally polarized beams,” Opt. Lett. **32**, 1468-1470 (2007).

[34] M. Stadler and M. Schadt, “Linearly polarized light with axial symmetry generated by liquid-crystal polarization converters,” Opt. Lett. **21**, 1948-1950 (1996).

[35] N. Passily, R. S. Denis, K. Ait-Ameur, F. Treussart, R. Hierle and J. F. Roch, “Simple interferometric technique for generation of a radially polarized light beam,” J. Opt. Soc. Am. A **22**, 984-991 (2005).

[36] S. C. Tidwell, G. H. Kim and W. D. Kimura, “Efficient radially polarized laser beam generation with a double interferometer,” Appl. Opt. **32**, 5222-5229 (1993).

[37] R. Zhao, T. Zhai, Z. Wang, Y. Wang and D. Liu, “Simultaneous excitation of cavity resonance and surface plasmon resonance in $Ag/Al_2O_3/Ag$ layer structure,” Appl. Phys. B **92**, 585-588 (2008).

[38] T. H. Lan, Y. K. Chung and C. H. Tien, “Broad detecting range of objective-based surface plasmon resonance sensor via multilayer structure,” Jpn. J. Appl. Phys. **50**, 09MG04 (2011).

[39] T. H. Lan, Y. K. Chung, J. E. Li and C. H. Tien, “Plasmonic rainbow rings induced by white radial polarization,” Opt. Lett. **7**, 1205-1207 (2012).